MEASUREMENTS OF DRAG TORQUE AND LIFT OFF SPEED

AND IDENTIFICATION OF STIFFNESS AND DAMPING IN A

METAL MESH FOIL BEARING

A Thesis

by

THOMAS ABRAHAM CHIRATHADAM

Submitted to the Office of Graduate Studies of
Texas A&M University
in partial fulfillment of the requirements for the degree of

MASTER OF SCIENCE

December 2009

Major Subject: Mechanical Engineering

MEASUREMENTS OF DRAG TORQUE AND LIFT OFF SPEED

AND IDENTIFICATION OF STIFFNESS AND DAMPING IN A

METAL MESH FOIL BEARING

A Thesis

by

THOMAS ABRAHAM CHIRATHADAM

Submitted to the Office of Graduate Studies of
Texas A&M University
in partial fulfillment of the requirements for the degree of

MASTER OF SCIENCE

Approved by:

Chair of Committee,	Luis San Andrés
Committee Members,	Alan B. Palazzolo
	Vikram K. Kinra
Head of Department,	Dennis L. O'Neal

December 2009

Major Subject: Mechanical Engineering

ABSTRACT

Measurements of Drag Torque and Lift Off Speed and Identification of Stiffness and Damping in a Metal Mesh Foil Bearing. (December 2009)

Thomas Abraham Chirathadam, B.Tech., National Institute of Technology Calicut, India

Chair of Advisory Committee: Dr. Luis San Andrés

Metal mesh foil bearings (MMFBs) are a promising low cost gas bearing technology for support of high speed oil-free microturbomachinery. Elimination of complex oil lubrication and sealing system by installing MMFBs in oil free rotating machinery offer distinctive advantages such as reduced system overall weight, enhanced reliability at high rotational speeds and extreme temperatures, and extended maintenance intervals compared to conventional turbo machines. MMFBs for oil-free turbomachinery must demonstrate adequate load capacity, reliable rotordynamic performance, and low frictional losses in a high temperature environment.

The thesis presents the measurements of MMFB break-away torque, rotor lift off and touchdown speeds, temperature at increasing static load conditions, and identified stiffness and equivalent viscous damping coefficients. The experiments, conducted in a test rig driven by an automotive turbocharger turbine, demonstrate the airborne operation (hydrodynamic gas film) of the floating test MMFB with little frictional loses at increasing loads. The measured drag torque peaks when the rotor starts and stops, and drops significantly once the bearing is airborne. The estimated rotor speed for lift-off increases linearly with increasing applied loads. During continuous operation, the MMFB temperature measured at one end of the back surface of the top foil increases both with rotor speed and static load. Nonetheless, the temperature rise is only nominal ensuring reliable bearing performance. Application of a sacrificial layer of solid lubricant on the top foil surface aids to reduce the rotor break-away torque. The measurements give confidence on this simple bearing technology for ready application into oil-free turbomachinery.

Impact loads delivered (with a soft tip) to the test bearing, while resting on the (stationary) drive shaft, evidence a system with large damping and a structural stiffness that increases with frequency (max. 200 Hz). The system equivalent viscous damping ratio decreases from ~ 0.7 to 0.2 as the frequency increases. In general, the viscous damping in a metal mesh structure is of structural type and inversely proportional to the frequency and amplitude of bearing motion relative to the shaft. Impact load tests, conducted while the shaft rotates at 50 krpm, show that the bearing direct stiffness is lower (~25% at 200 Hz) than the bearing structural stiffness identified from impact load tests without shaft rotation. However, the identified equivalent viscous damping coefficients from tests with and without shaft rotation are nearly identical.

The orbits of bearing motion relative to the rotating shaft show subsynchronous motion amplitudes and also backward synchronous whirl. The subsynchronous vibration amplitudes are locked at a frequency, nearly identical to a rotor natural frequency. A backward synchronous whirl occurs while the rotor speed is between any two natural frequencies, arising due to bearing stiffness asymmetry.

ACKNOWLEDGEMENTS

NOMENCLATURE

$\{a_i\}_{i=X,Y}$	Acceleration of bearing cartridge along X and Y directions [m/s^2]
C_{crit}	Critical damping [Ns/m]
D	Diameter of rotating shaft [m]
D_{Bi}	Bearing cartridge inner diameter [m]
D_{Bo}	Bearing cartridge outer diameter [m]
D_{MMi}	Metal mesh ring inner diameter [m]
D_{MMo}	Metal mesh ring outer diameter [m]
D_W	Metal wire diameter [m]
E	Young's Modulus [N/m^2]
f	Friction coefficient [-]
$\{f_i\}_{i=X,Y}$	External excitation force [N]
f_n	Test system natural frequency [Hz]
F_Y	Impact force in frequency domain [N]
$\{K_{ij}, C_{ij},\}_{i,j=X,Y}$	Bearing stiffness [N/m] and equivalent viscous damping coefficients[Ns/m]
L	Bearing axial length [m]
M	MMFB mass [kg]
M_m	Metal mesh ring mass [kg]
P	Power loss [W]
R	Radius of the rotating shaft [m]
R_i	Metal mesh ring inner radius [m]
R_o	Metal mesh ring outer radius [m]
T_{tf}	Top foil thickness [m]
U_d, U_v, U_f	Uncertainty in displacement[mm], voltage[V] and force [lb] respectively
W	Total static load on the bearing [N]
W_S	Applied static load [N]
W_D	Dead weight of the bearing assembly [N]

ρ_{MM}	Wire density = metal mesh mass/ (metal mesh volume× density of metal)
υ	Poisson's Ratio
ω	Excitation frequency [Hz]
$\{\delta i\}_{i=X,Y}$	Relative displacement of bearing with respect to the rotating shaft [m]
γ	Loss factor [-]

TABLE OF CONTENTS

Page

LIST OF FIGURES

LIST OF TABLES

CHAPTER I

INTRODUCTION

Oil-free microturbomachinery (< 250 kW) implements gas bearings as they offer distinctive advantages like low friction, absence of complex lubrication systems, reliability and long operating life with little need of maintenance [1]. In a gas foil bearing, the hydrodynamic pressure generated within a small gap between the rotating shaft and a smooth foil supports a load. Gas foil bearings are presently used in air cycle machines, cryogenic turbocompressors and turboexpanders, and micro gas turbines. Gas bearings have potential application in high speed rotor bearing systems with moderate loads (static and dynamic) such as in fuel cell electric power systems, automotive turbochargers, etc [2].

Metal mesh foil bearings (MMFB) comprise of a top foil supported on a ring shaped metal mesh (MM) providing structural stiffness and mechanical energy dissipation with material hysteresis or dry-friction [3]. The current research on MMFBs modifies a patented gas bearing with an elastic porous material underneath a smooth top foil [4]. Figure 1 taken from Ref. [4] shows that the bearing consists of a bearing cartridge (a), an external circular (cartridge shim) foil (b), a resilient porous material support (c), and a top circular smooth foil (d). The trailing edges of the top circular foil, porous material and external circular (cartridge shim) foil are pinned at (g) and the top foil leading edges are free. The external circular (cartridge shim) foil facilitates seamless installation of the porous material inside the bearing cartridge. As the rotor (e) speed increases, a hydrodynamic film pressure (f) builds up and separates the rotor from the top foil.

Metal mesh foil bearings aim to satisfy the requirements for light, inexpensive, high power density (power per unit mass) gas turbines and automobile turbochargers, for example. The elimination of lubricating oil in MMFBs enhances the bearing reliability at high rotational speeds and extreme temperatures. MMFBs for oil-free turbomachinery

---

This thesis follows the style of the ASME Journal of Engineering for Gas Turbines and Power.

require of adequate load capacity, reliable rotordynamic performance, and low frictional losses in a high temperature environment.
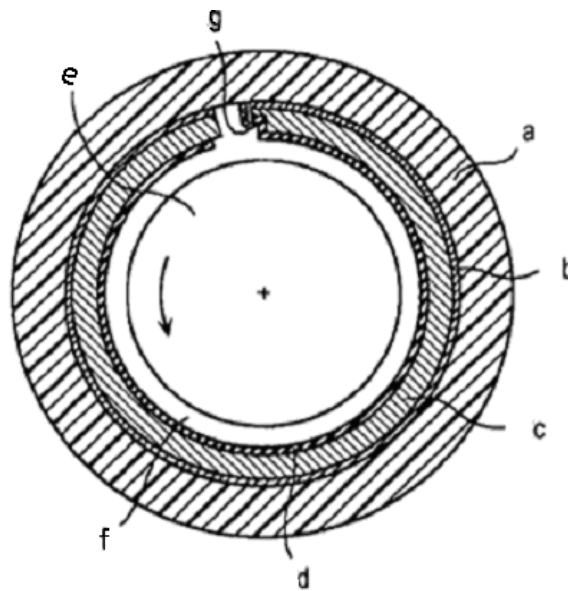
Fig. 1 Air foil bearing with a porous material support [4], (a) bearing cartridge, (b) external circular (cartridge shim) foil, (c) porous material support, (d) top circular foil, (e) rotating shaft, (f) hydrodynamic air film and (g) pinned edge. Patent No. WO 2006/043736 A1

The current metal mesh foil bearing design follows the concept illustrated in Figure 1, but installs a commercially available metal mesh ring between the top foil and the bearing cartridge, as depicted in Figure 2, to provide structural stiffness and damping. Note that prior experiments conducted at the Turbomachinery laboratory (TL) have demonstrated that metal mesh materials render equivalent viscous damping large enough to replace oil-lubricated squeeze film dampers, for example [5].
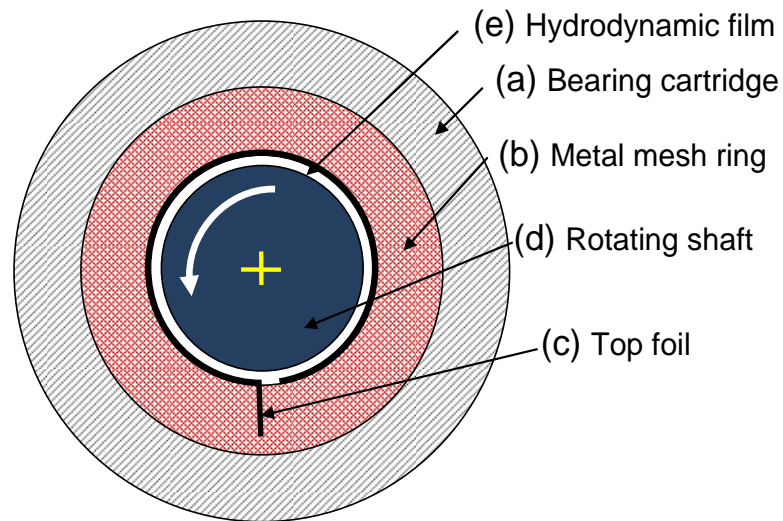
Fig. 2 Schematic view of a metal mesh foil bearing

San Andŕes et al. [6] present the estimated structural stiffness and damping of a MMFB, obtained from static and dynamic load tests. Static load versus bearing deflection measurements show a nonlinear load-deflection relationship with a large mechanical hysteresis, indicating large mechanical energy dissipation. As depicted on Figure 3, the estimation of bearing stiffness, using the real part of the transfer function and bearing mass from a curve fit of the test data, shows an increase (~ 15 %) in magnitude with an increase in frequency from 25 to 400 Hz, and decrease (~50%) with an increase in amplitude of motion from 12.7 μm to 38.1 μm. At the lowest test frequency of 25 Hz, the equivalent viscous damping coefficient attains the highest magnitude (~3.5 kNs/m and 2 kNs/m for 12.7 μm and 38.1 μm motion amplitudes respectively). Figure 4 shows that the equivalent viscous damping coefficient decays exponentially for increasing test frequencies. For the entire range of test frequencies, the MMFB equivalent viscous damping reduces with increase in motion amplitudes. The stiffness and equivalent viscous damping predictions, using empirical equations from Ref. [7], show good agreement with identified parameters. The hysteretic damping property of the metal mesh ring is best represented with a loss factor (γ) defined as the ratio of the imaginary part of the mechanical impedance to the bearing stiffness. Figure 5

shows that the identified loss factor is as high as 0.7, a large magnitude for the simple bearing configuration, and exhibits little dependency on excitation frequency. However, experiments over a period of time show a reduction in MMFB stiffness and damping coefficients after multiple dismantling and reassembly processes and continuous operation.
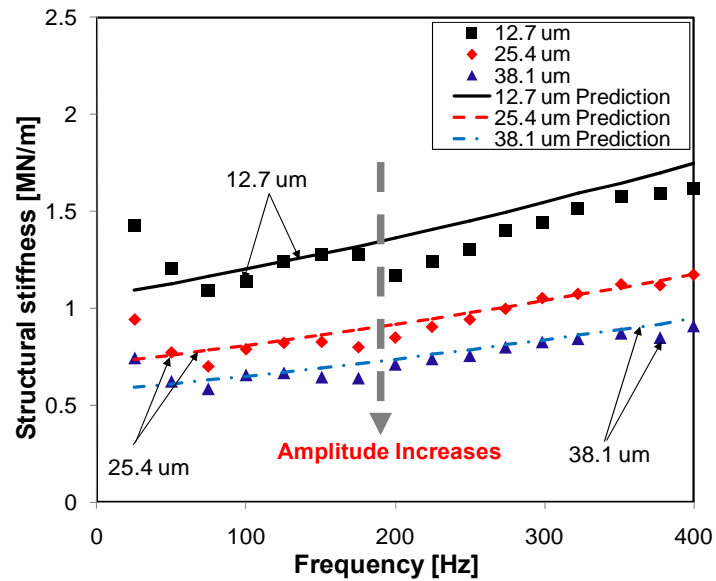
Fig. 3 MMFB structural stiffness *(K)* **versus frequency derived from three motion amplitudes (12.7 µm, 25.4 µm, 38.1 µm). Ref. [6]**
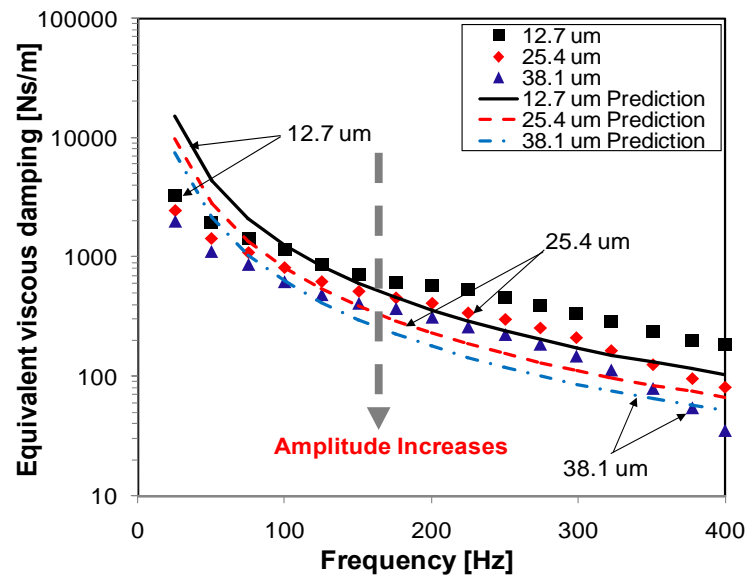
Fig. 4 Equivalent viscous damping versus frequency of excitation derived from three motion amplitudes (12.7 µm, 25.4 µm, 38.1 µm). Ref. [6]
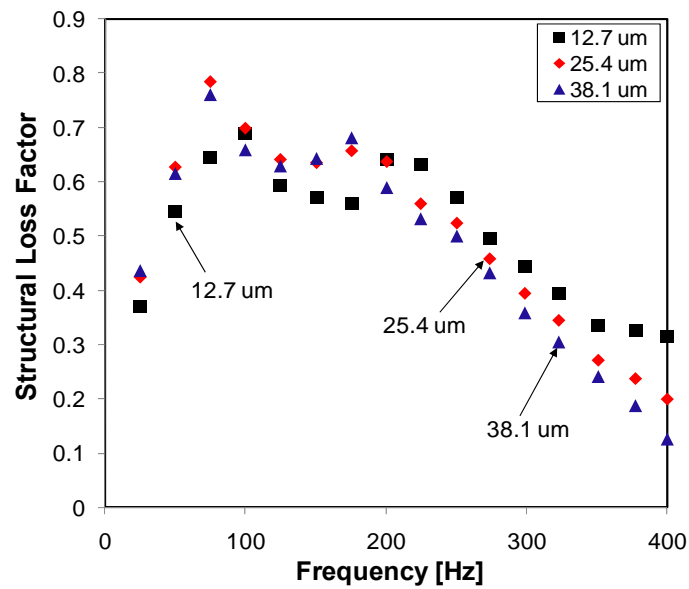
Fig. 5 Structural loss factor (γ) versus frequency of excitation derived from three motion amplitudes (12.7 µm, 25.4 µm, 38.1 µm). Ref. [6]

The present work advances prior research [6] by measuring the dynamic forced response of MMFBs. The bearing stiffness and damping coefficients are estimated from the rotor response to impact loads. The test bearing floats on a journal press fitted on the shaft stub of a turbocharger. Eddy current sensors measure the motion of the test journal relative to the bearing along two orthogonal directions. The measurement of bearing drag torque, temperature rise and load capacity for various static loads and operating speed conditions will provide the information required for the application of metal mesh foil bearings in oil-free rotating machinery.

CHAPTER II
LITERATURE REVIEW

This literature review discusses prior work on the experimental identification and prediction of i) Metal Mesh damper force coefficients and ii) load capacity of foil bearings and various techniques implemented to improve foil bearing load capacity.

METAL MESH DAMPER

Metal mesh dampers are a promising candidate for providing the support stiffness and damping in gas foil bearings. The major advantage of metal mesh damper is its usability in high and low temperatures. Since the 1980's, metal mesh materials have been employed as vibration isolators [8] in gas turbine engines. A ring shaped metal mesh damper, installed in series with the outer race of an engine bearing, can provide a soft support to the turbine shaft without the need of any stiffening element. Recent work [5] also demonstrates that ring shaped metal mesh dampers provide equivalent viscous damping as large as that of oil-lubricated squeeze film dampers. The following summarizes literature on metal mesh vibration isolators and dampers.

Okayasu et al. [9] report one of the earliest use of metal mesh, as a flexible bearing support in a liquid hydrogen turbopump, for controlling subsynchronous instability arising due to dry friction between rotating parts. The introduction of metal mesh dampers reduces high level of vibrations while traversing critical speeds. The turbopump was designed to operate above its third critical speed of 46,139 rpm. In the absence of metal mesh dampers, high vibration levels (80-150 μm pk-pk) were measured while crossing the first and second critical speeds. Introduction of metal mesh dampers in the rotor-bearing system attenuated synchronous and subsynchronous vibrations.

Zarzour [5] introduces a stainless steel mesh damper replacing a squeeze film damper (SFD) as an effective damping element. Experiments in a test rig replicating a power turbine demonstrate that the viscous damping coefficients of the metal mesh dampers were comparable to that of SFDs. The viscous damping coefficient of the metal mesh damper did not change significantly for tests covering a temperature range of

54°C-99°C, proving its reliability as a damping element in this temperature range. However, the stiffness decreases (softening effect) with an increase in operating temperature. Also, the imbalance response amplitude at the rotor-bearing system critical speed does not change when the metal mesh is drenched in oil. Note that the metal mesh damper shows, during static load tests, a peculiar behavior with linear loading and non-linear unloading features. That is, during loading, the metal mesh ring deflection is linear; and during unloading, the metal mesh ring deflection is nonlinear.

Metal mesh dampers retain its damping when assembled in conjunction with other stiffening elements. Al-Khateeb and Vance [10] report that a ring shaped metal mesh damper in parallel with a squirrel cage, a stiffening member, allows varying the support stiffness without any effect on its equivalent viscous damping. Ertas et al. [11] investigate the usefulness of metal mesh as bearing dampers at cryogenic temperatures, reporting an increase in metal mesh damper stiffness with a decrease in temperature for both steel and copper meshes. The equivalent viscous damping coefficient of a steel mesh damper does not change with temperature. However, the equivalent viscous damping increases significantly for a copper mesh damper with a decrease in temperature, achieving its highest value at the lowest test temperature of -190°C. The selection of the mesh material depends mainly on the damping it provides. Burshid [12] reports using a copper mesh for auxiliary sealing in a hybrid damper seal design. Tests show that a copper wire mesh exhibits more damping than a stainless steel wire mesh.

Knowledge of the physical parameters affecting the viscous damping and stiffness of a metal mesh damper is necessary for its engineered design and scalability. Al-Khateeb [3] finds that dry friction and at least one more source of damping, possibly material hysteresis, influence the overall viscous damping of a metal mesh ring damper. Dynamic load tests on a metal mesh damper demonstrate frequency – amplitude dependent stiffness and equivalent viscous damping coefficients, i.e., a nonlinear forced performance. Choudhry and Vance [7] report design equations, empirically based, to predict stiffness and viscous damping coefficients of metal mesh ring dampers. The effective Young's Modulus of a metal mesh ring depends on the ring geometry and

metal mesh compactness ratio. Hence the design equations, with stiffness and viscous damping coefficients as functions of metal mesh ring geometry and compactness ratio, identifies the metal mesh effective Young's Modulus using simple tests, at any specified excitation frequency.

Ao et al. [7] reports estimating the stiffness and damping coefficients of a steel mesh damper, typically used in aerospace industry, by applying external rotary forces on the damper. The study shows that the metal mesh compactness and the direction of loading significantly affect the damping performance of the material. Ao et al. [7] further investigates the effect of unidirectional and bidirectional loading on the damping performance of metal meshes based on the Masing model [13]. The experiments show that the amplitude of deformation and the frictional forces from other directions also affect the damping offered by the metal mesh ring. Experimental studies by Hou et al. [14] display bending and leaping in the transmissibility curves for metal meshes indicating the presence of higher order restoring force components. The authors report loss factors decreasing rapidly with increasing frequencies. The authors mention that the Coulomb friction between wires reduces at high vibration frequency and hence the dissipation of energy due to friction is less at large frequencies of operation. The loss factor, however, does not show any clear trend with temperature.

Metal mesh dampers display nonlinear stiffness and viscous damping properties which make their prediction difficult. Ertas and Luo [15] report characterizing the nonlinear stiffness and damping of metal mesh rings by varying the vibration amplitude, excitation frequency, and static eccentricity. The tests show that the eccentricity (due to a static load) has no influence on the damper force coefficients. Also, maximum viscous damping is present at the lower frequency ranges (0-50 Hz) and the viscous damping coefficient reduces from ~29 kNs/m (at 20 Hz) to ~3.5 kNs/m (at 300 Hz). The authors successfully demonstrate low rotor vibration levels through the first two critical speeds during high-speed tests with metal mesh ring as damping element.

Recently, Ertas [16] report a novel compliant hybrid journal bearing for enabling oil-free operation in high speed turbomachinery. The design integrates a flexurally supported

multiple pad hybrid bearing and two metal mesh rings, inserted under the pads at the bearing sides, maximizing load carrying capacity and effective damping without sacrificing compliance to misalignment between rotor and bearing. Test data show that the viscous damping decreases with increasing excitation frequency. The bearing direct stiffness decreases with increasing frequency with no external pressure applied into the bearing pads. But, with an applied feed pressure, the bearing direct stiffness shows an increasing trend with increasing frequency. Also, the subsynchronous vibration components, present in rotordynamic tests without the dampers, are absent at the system natural frequency with the metal mesh dampers installed.

LOAD CAPACITY OF FOIL BEARING

In 1897, Kingsbury introduced the first self-acting air journal bearing [17], in which a minute hydrodynamic air film formed between the bearing and its rotating shaft supports a load. In 1953, Block and Van Rossum [18] presented the compliant surface foil bearing that has a larger hydrodynamic film thickness compared to rigid gas bearings, increasing its operational reliability and removing the stringent requirement for tight manufacturing clearances. Agrawal [1] presents an overview of foil bearing technology summarizing its chronological development during the last quarter of the 20th century. The author lists several applications of foil gas bearings like air cycle machines, vapor cycle machines, cryogenic turbo pumps, high speed fans for space stations, turbo expanders, high temperature auxiliary power unit for aircrafts, and a missile engine incorporating hot end foil bearings. The successful application of a foil bearing technology in high speed oil-free machinery requires of low drag torque, during start up and shut down, and sufficient load carrying capacity in the typical operating range of 20 – 70 krpm.

DellaCorte and Valco [19] introduce an empirically based 'rule of thumb' relating the bearing load capacity to the bearing size and rotor speed. The earliest bump type foil bearings (Generation I) have a low load because of their single bump foil strip with near uniform stiffness in the radial and circumferential directions. Generation II bearings with bump strips designed for a circumferentially varying stiffness double the load capacity.

Further optimization of the bump strip layers with varying radial stiffness (Generation III) shows a more than two fold increase in load capacity. Advanced foil bearings, with compliance tailored elastic support structures, exhibit load capacities up to five times that of the initial simple designs.

DellaCorte [20] presents a high temperature test rig to measure the drag torque in foil bearings during multiple startup and shutdown cycles and reaching rotational speeds to 70 krpm. The test bearing has inner diameter and length of 35 mm and 25 mm, respectively. The test results show that the bearing drag torque is large just before rotor lift off, and immediately after rotor touchdown, due to rubbing contact between the journal and the top foil surface. Once the bearing is airborne, the drag torque reduces to a minimum, and then increases gradually with rotor speed. In further tests in Ref. [21], the foil bearing torque increases with static load and decreases with operating temperature. The frictional force and contact stress between the top foil and the shaft surface contributes to the large drag torque at start up. The load capacity is estimated by coasting down the rotor from a high speed, while a static load is applied on the foil bearing, until the drag torque suddenly rises indicating the onset of rubbing. In a gas bearing, the load capacity approaches a limit, not increasing further with surface speed. The experimental load capacity in the test bearing is linear with speed to 30 krpm. It is speculated that a foil bearing reaches its ultimate load capacity when the minimum film thickness approaches the combined surface roughness of the top foil and the rotating shaft [21]. In the tests, the foil bearing load capacity decreases with increasing operating temperature, possibly due to the decrease in the support structure stiffness. Note that the ultimate load capacity of a foil bearing cannot exceed that of its resilient support structure, i.e. the bump strip layers.

Radil et al. [22] reports that the load capacity of a Generation III foil bearing, with inner diameter of 35 mm and length 25 mm and constructed from several nickel based super alloy foils, is the highest for a near optimum clearance. Note that clearance in a foil bearing is a vague concept since in actuality, upon assembly, no physical gap exists between a top foil and a stationary shaft. Continuous operation of a foil bearing that has

a suboptimal clearance results in thermal runaway failure and seizure. However, a foil bearing can be operated safely with a radial clearance larger than the optimal value, but at a reduced load capacity. Ref. [23] shows that tailoring the support structure, to reduce the side leakage and to provide a uniform film thickness, results in a higher load capacity.

Peng and Khonsari [24] determine the ultimate load capacity of ideal foil bearings, showing its dependency on the stiffness (compliance) of the support structure beneath the top foil. Kim and San Andŕes [25] further advance the analysis to determine the effect of assembly preload on the ultimate load capacity for gas foil bearing operation at ultra high operating speeds. Note that foil bearings are typically assembled with a slight preload, i.e., the inner diameter of the top foil bring smaller than the journal diameter.

The current research does not focus on the tribological characteristics [26, 27] of solid lubricant coatings on the top foil and the rotating shaft.

CHAPTER III

DESCRIPTION OF TEST BEARING AND EXPERIMENTAL FACILITY

TEST METAL MESH FOIL BEARING

Figure 6 shows the photograph of a prototype bearing and Table 1 describes the three main components comprising a MMFB. The MMFBs employ commercially available ring shaped metal mesh as the elastic support under a thin top foil. The prototype bearing uses a metal mesh ring made of copper wires, owing to the large structural damping offered by copper meshes [3]. The top foil, a smooth arcuate surface 127μm thick, is in contact with the journal when not in operation. Note that, at high rotor speed operation, a thin hydrodynamic air film separates the top foil and the rotating journal. Hence, any wear of the journal or the bearing is absent while the rotor is airborne. In MMFBs, the metal mesh supporting the top foil also provides material damping and dry-friction energy dissipation effects [3].

The top foil is made from a cold rolled steel strip (Chrome-Nickel alloy, Rockwell 40/45) with significant resilience to deformation. The steel strip is first heat treated in a die at a temperature of 927° C and then allowed to cool for ~ 10 hours. Further, a tempering process at ~ 400 ° C toughens the formed top foil. The heat treatment process follows the recommendations in Ref. [14] that details the heat treatment processes typically employed in the manufacturing of top foils in commercial bearings.
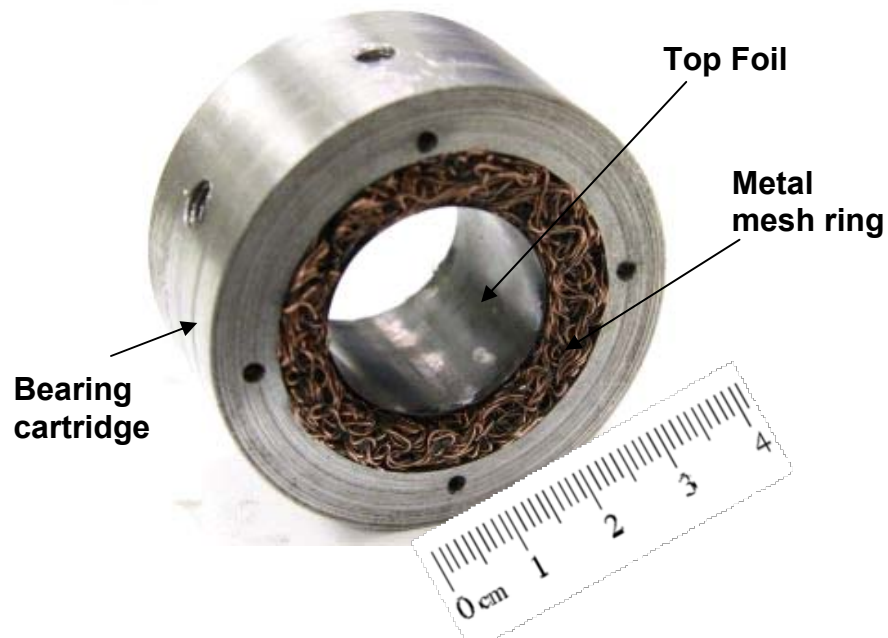
Fig. 6 Photograph of a metal mesh foil bearing manufactured at TAMU

Table 1. Description of metal mesh foil bearing components

	Description	Role
Bearing Cartridge	Stainless steel cylindrical ring	Cartridge holding metal mesh ring and smooth top foil.
Metal mesh ring (MM)	Ring shaped compressed woven wire mesh	Soft material support provides structural stiffness and energy dissipation
Smooth top Foil	Thin Stainless steel sheet, curved and preformed, with one end affixed to the metal mesh ring and the other end free.	A hydrodynamic film pressure builds up within the gap between the rotating shaft and the top foil.

Figure 7 displays a schematic representation of a cross sectional view of the test MMFB and illustrates the installation of the smooth arcuate top foil inside the metal mesh ring. One end of the top foil has two identical shaped tabs that are bent and fit into the two apertures inside the ring shaped metal mesh during assembly. After affixing the

top foil into the metal mesh, the assembly is inserted into the bearing cartridge to complete the construction of the MMFB [6]. A thin and uniform solid lubricant coating of MoS_2 is applied on the top foil inner surface to protect it from excessive wear due to frictional contact with the rotating journal. Table 2 displays the dimensions of the MMFB with the metal mesh ring inner diameter of 28.30 mm and axial length of 28.05 mm. Cooper wire with a diameter of 0.30 mm comprises of a metal mesh ring with a compactness of 20%. The compactness (wire density) of the metal mesh determines its physical (equivalent) properties [3]. Stainless steel top foil thickness is 0.127 mm. The total mass of MMFB including a torque arm (see Fig. 8) is ~ 0.363 kg.

Bearing Cartridge

Metal Mesh Ring

Top Foil

D_{MMi} D_{Bi} D_{Bo}

Tabs

L
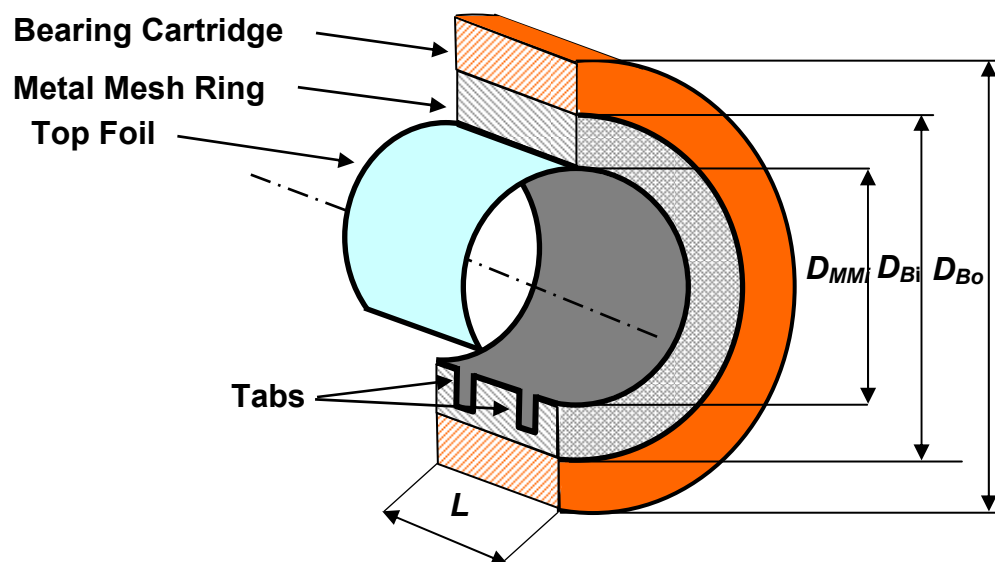
Fig. 7 Schematic representation of cut view of the MMFB

Table 2. Nominal dimensions and material specifications for test MMFB

Parameter name and physical dimension	Magnitude
Bearing cartridge outer diameter, D_{Bo} (mm)	58.15 ± 0.02
Bearing cartridge inner diameter, D_{Bi} (mm)	42.10 ± 0.02
Bearing axial length, L (mm)	28.05 ± 0.02
Metal mesh outer diameter, D_{MMo} (mm)	42.10 ± 0.02
Metal mesh inner diameter, D_{MMi} (mm)	28.30 ± 0.02
Metal mesh mass, M_m (kg)	0.0391
Metal mesh density, ρ_{MM} (%)[1]	20
Top foil thickness, T_{tf} (mm)	0.127
Wire diameter, D_W (mm)	0.30
Copper Young modulus, E (GPa), at 21 ºC [28]	114
Copper Poisson ratio, υ [29]	0.33
Bearing mass (cartridge + mesh + foil + torque arm), M (kg)	0.363

Uncertainty in mass measurement = ± 0.0001 kg

EXPERIMENTAL FACILITY

Figure 8 shows a photograph of the test rig with a ball bearing supported turbocharger (TC) turbine driving the system to a maximum speed of 120 krpm. The compressor impeller and volute of the original TC are removed to expose the overhanging shaft. A journal of diameter 28 mm and length 55 mm is press fitted on the TC shaft end and fastened with a nut. The journal is balanced in-place using correction masses inserted at eight equally spaced threaded holes on the journal front face. The MMFB slides on the journal and remains afloat when the journal starts rotating. A torque arm attached to the bearing prevents its rotation.

---

[1] Manufacturers define the density of metal mesh as the ratio of the ring mass to its volume times the metal material density.
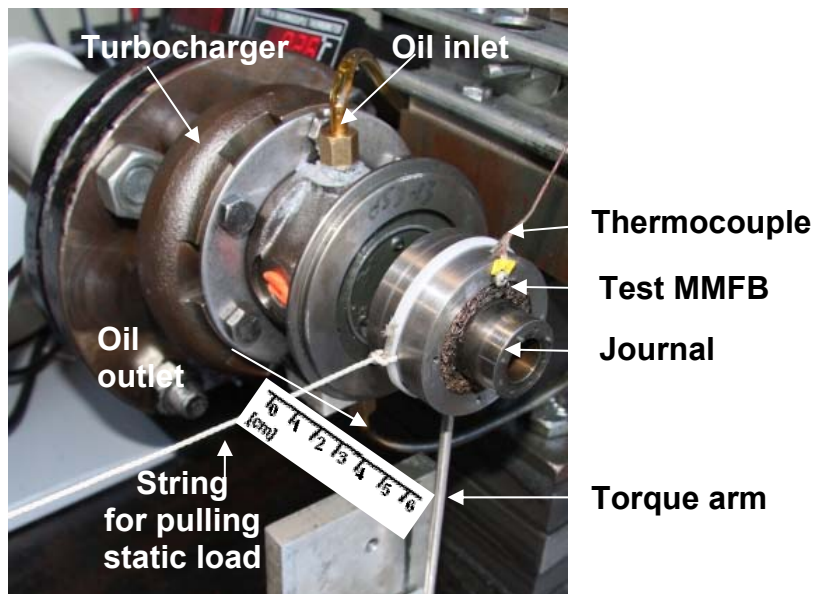
Fig. 8 Photograph of test rig with metal mesh foil bearing mounted on journal (28 mm diameter and 55 mm length)

Figure 9 shows a schematic front view of the test bearing, journal, and the devices for measurement of torque, applied load and temperature. Once the journal starts rotating, the torque arm applies a force on the soft spring (0.88 kN/m), and the spring reaction force balances the drag moment acting on the bearing. An eddy current sensor records the lateral displacement of the torque arm. The rubber band shown gives a slight preload and prevents axial motions of the test bearing.

Static (horizontal) loads are applied on the bearing by pulling a string (flexible) connected to the bearing, using a positioning table. A dynamometer ($\pm$ 0.2 N) affixed to the linear positioning table measures the applied load. As the positioning table moves toward left, as illustrated in Figure 9, the string applies a horizontal load on the bearing floating on the shaft. Note that the string, loosely wound around the bearing circumference (at its axial mid-plane) does not prevent the bearing rotation, thus facilitating seamless torque measurement. Incidentally, note that the weight of the bearing assembly is 3.5 N. A K-type thermocouple affixed at one of the bearing ends

measures the top foil temperature (± 0.5 °C). An infrared tachometer, mounted within the safety structure, measures the turbine tip speed with ± 0.0015 % accuracy.
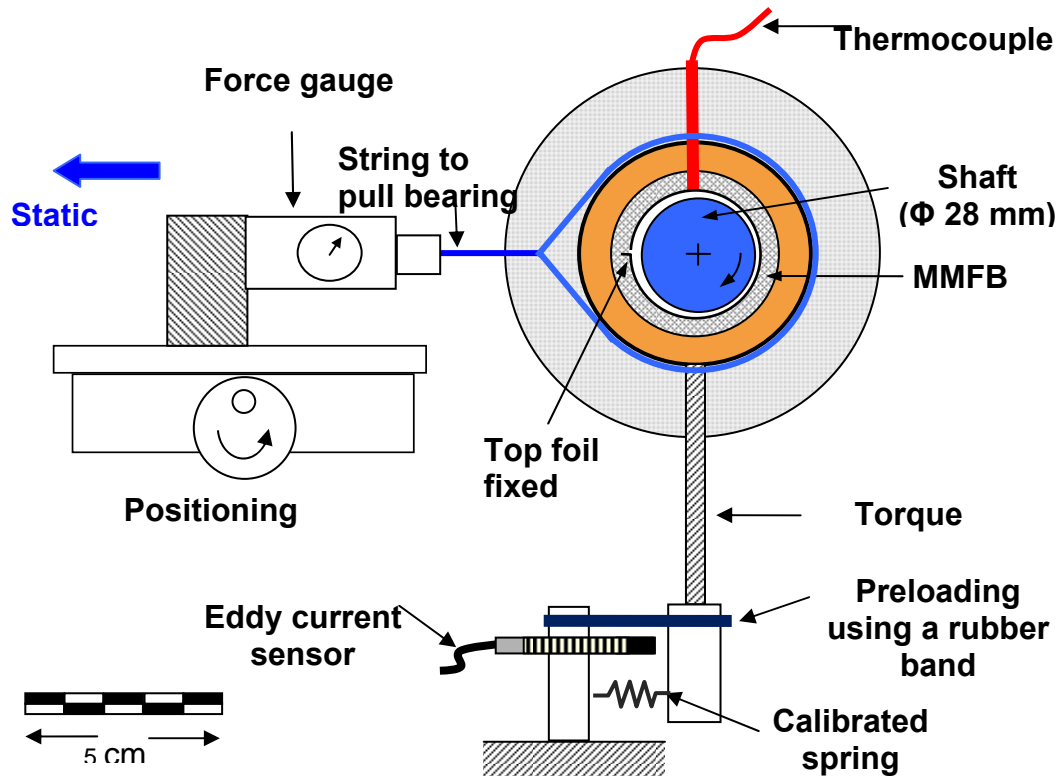
Fig. 9 Schematic view of MMFB, rotating journal, and instrumentation for static (pull) load and torque measurements

A pressure regulator adjusts the supply air pressure [8.1 bar (120 psig) max.] into the turbine inlet. A ball valve throttles the inlet air and the exhaust air is routed from the test cell to the outside environment. The gradual increase of the inlet air into the turbine accelerates the rotor to a certain steady state speed. Further, depending on the test type, either the inlet air is suddenly cut or gradually reduced (stepwise), the rotor speed decreases until it stops rotating.
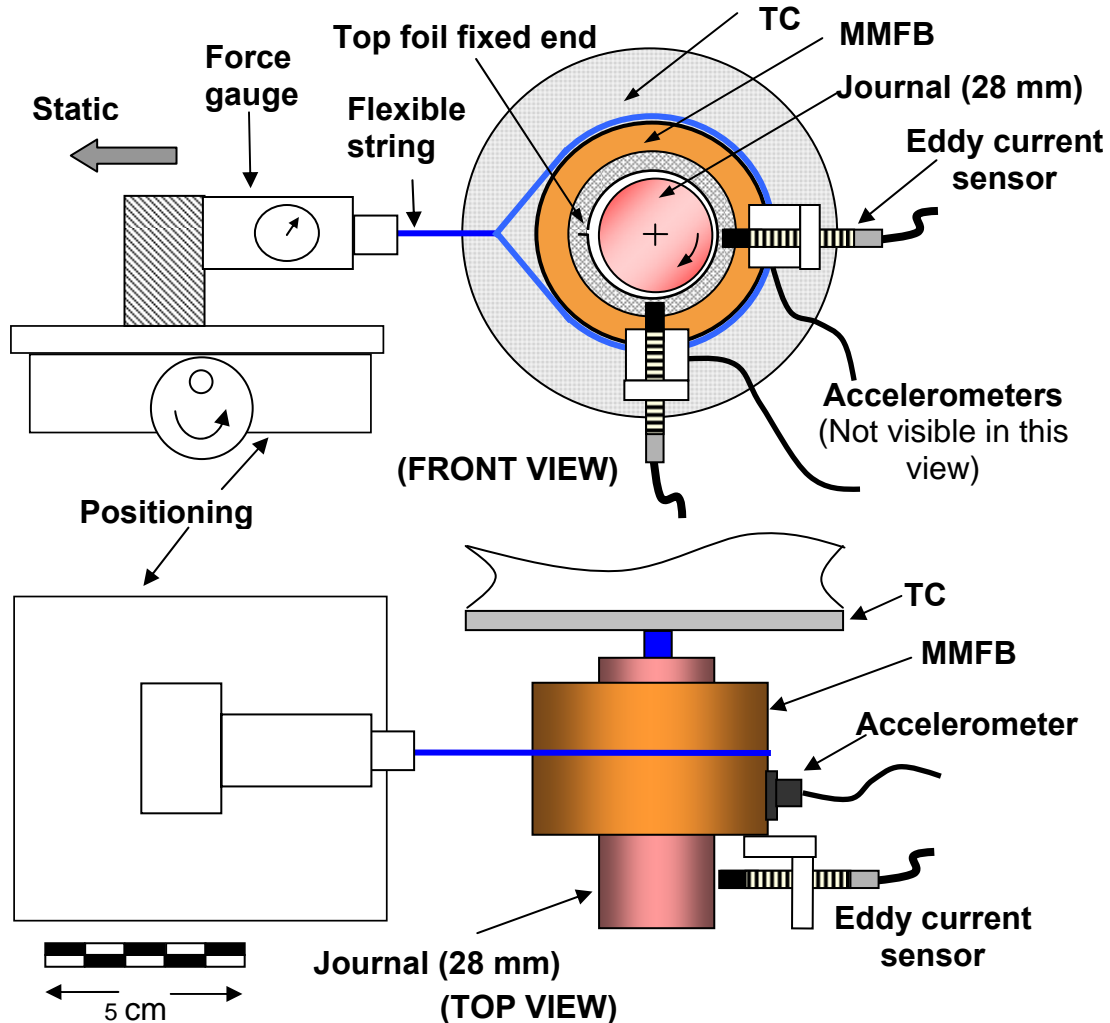
Fig. 10 Schematic views of MMFB mounted on shaft of turbocharger drive system. Sensors for measuring bearing accelerations and displacements relative to shaft (horizontal and vertical directions) shown

The torque arm is later removed and two eddy current sensors and two miniature piezoelectric accelerometers (each weighing 5.1 g), as shown in Figure 10, are affixed to the test bearing along orthogonal directions for measuring the bearing motion while the shaft (journal) spins.

CHAPTER IV

MEASUREMENT OF DRAG TORQUE, LIFT-OFF SPEED, AND TOP FOIL TEMPERATURE IN A METAL MESH FOIL BEARING

MEASUREMENT OF BEARING DRAG TORQUE

The air inlet valve is controlled to accelerate the TC shaft from rest, maintain it at a steady speed, and then decelerate it to rest as the air valve is closed. Figure 11 shows the journal speed and bearing drag torque versus time during a lift-off test cycle with an applied static (pull) load of 17.8 N (4 lb). The rotor accelerates beyond the bearing lift of speed (~ 28 krpm) to a steady speed of 65 kprm, and then decelerated to rest. As the rotor starts to spin, rubbing between the journal and top foil surfaces generate a sharp peak in bearing torque (~ 110 N-mm). Once the journal starts rotating, the torque falls rapidly. Further, the bearing operates in a mixed lubrication regime with partial asperity contacts, until the thin air film completely separates the two surfaces. The airborne journal, at a steady speed of 65 kprm, offers a significantly smaller drag torque of ~ 3.2 N-mm, i.e. 3% of the peak (break-up) torque. While decelerating to rest, the journal comes into physical contact with the top foil and causes a sharp peak in the drag torque (80 N-mm).

The lift-off shut-down test cycle is again conducted with a step wise change in the rotating speed. Figure 12 shows the rotor speed and bearing drag torque versus time with an applied static load of 8.9 N (2 lb). Note that the (horizontal) direction of the static pulling load (WS) is 90° away from that of the bearing dead weight (WD=3.5 N). Hence, the total static load acting on the MMFB is $W = \sqrt{W_S^2 + W_D^2}$ [2].The opening of the valve instantly brings the rotor to 65 krpm, overcoming a dry friction torque, due to rubbing with the top foil, of 57 N-mm. Once airborne, the viscous drag torque, between the air film and the top foil, is only 2.5 N-mm. Next, after every 20 s, the air inlet valve to the

---

[2] Total static load is 9.6 N, 18.2 N, 26.9 N, and 35.8 N for the applied (horizontal) static loads of 8.9 N, 17.8 N, 26.7 N, and 35.6 N, respectively.

turbine is closed a little more, to reduce the rotor speed in a stepwise manner. The drag torque decreases with journal speed, to 2.4 N-mm at 50 krpm, to 2.0 N-mm at 37 krpm, to 1.7 N-mm at 24 krpm, respectively. Further reduction in the rotor speed evidences an increase in drag torque. The drag torque peaks to 45 N-mm just before the rotor comes to rest.
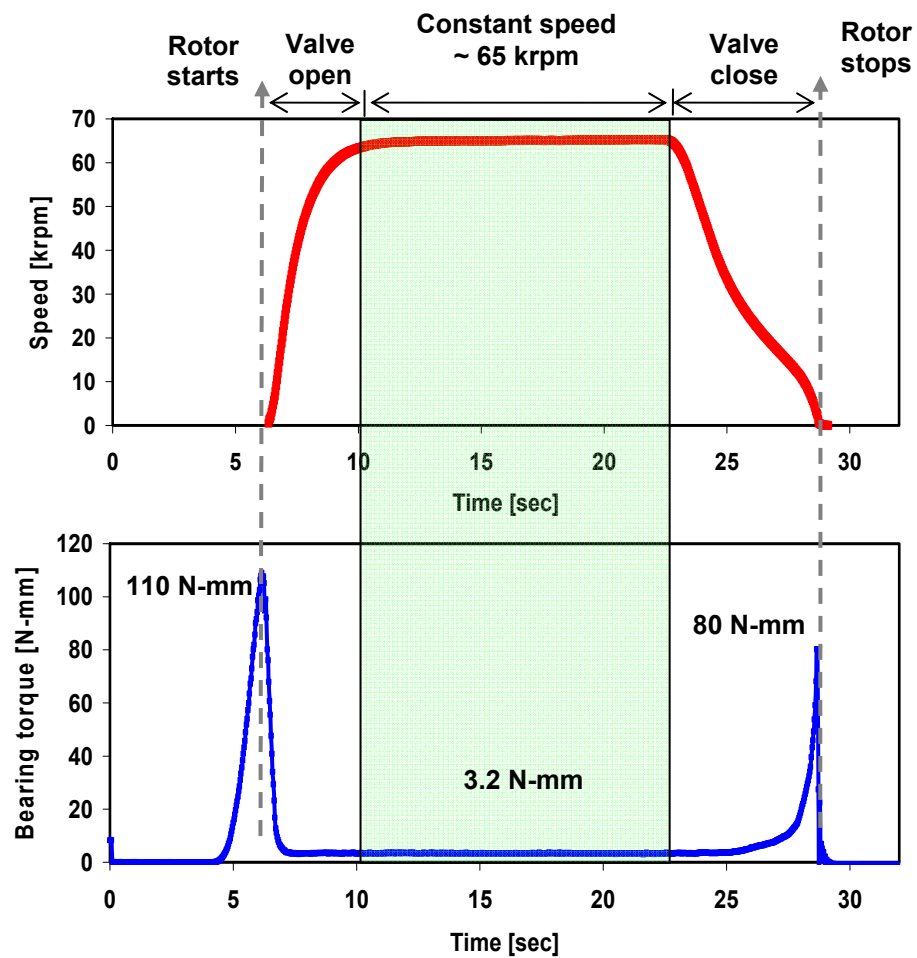
Fig. 11 Rotor speed and bearing torque versus time during a lift-off test cycle for applied static load of 17.8 N (4 lb). Manual speed-up to 65 krpm, operation at a constant rotor speed of 65 krpm, and deceleration to rest

Bearing lift-off tests with stepwise variation in rotor speed, as shown in Figure 12, are repeated for increasing static loads (18.2 N, 26.9 N, and 35.8 N). Figure 13 depicts the steady state (viscous) drag torque while the bearing is airborne. The bearing drag torque increases with increasing rotor speed and static loads. For static loads larger than 18.2 N, the rotor lift-off speeds are above 35 krpm.
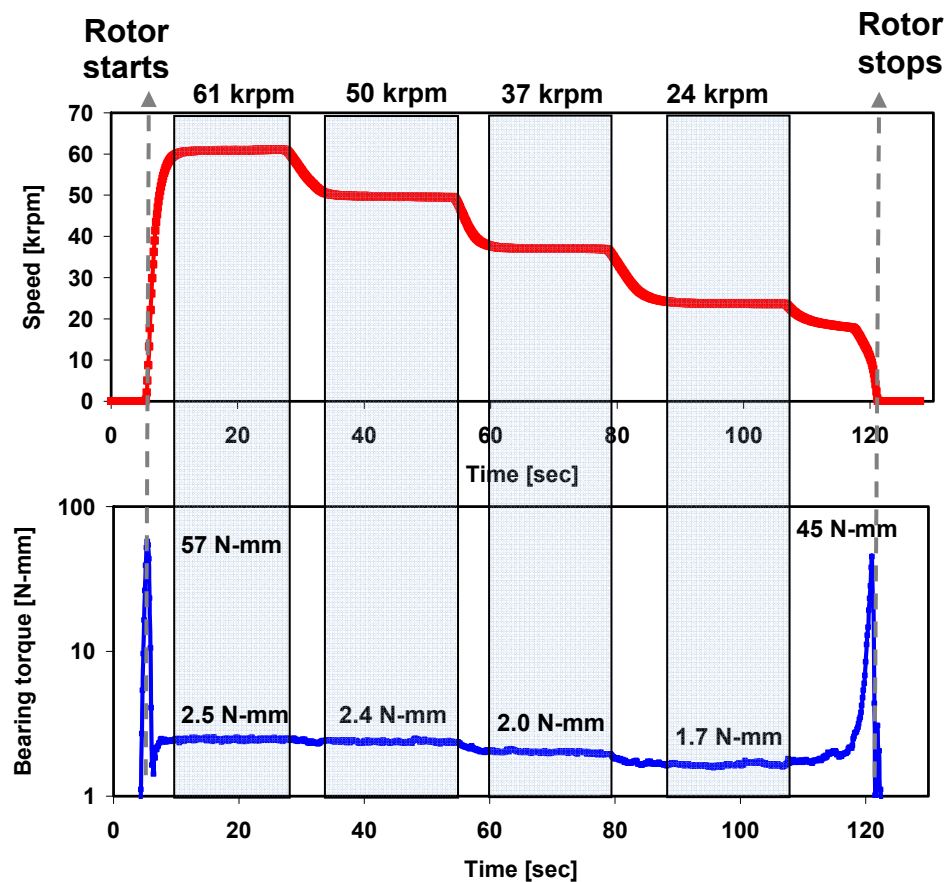
Fig. 12 Rotor speed and bearing torque versus time during a lift-off test cycle with scheduled variations in speed. Applied static load of 8.9 N (2 lb). Manual speed-up to 61 krpm, operation at fixed rotor speeds of 60, 50, 37, 24 krpm and deceleration to rest

Figure 14 shows the friction coefficient (*f*) derived from the data in Figure 13. Recall that $f = Torque / (WR)$ with $R = \frac{1}{2}D = 14$ mm is the journal radius. As expected, the

friction coefficient is nearly proportional to the rotor speed. However, the friction coefficient decreases as the static load increases. The highest friction factor of 0.018 is recorded for the smallest load (8.9 N) at the top speed of 61 krpm. The friction coefficient due to the hydrodynamic viscous drag is quite small. Hence, the MMFB when airborne offers negligible power losses.
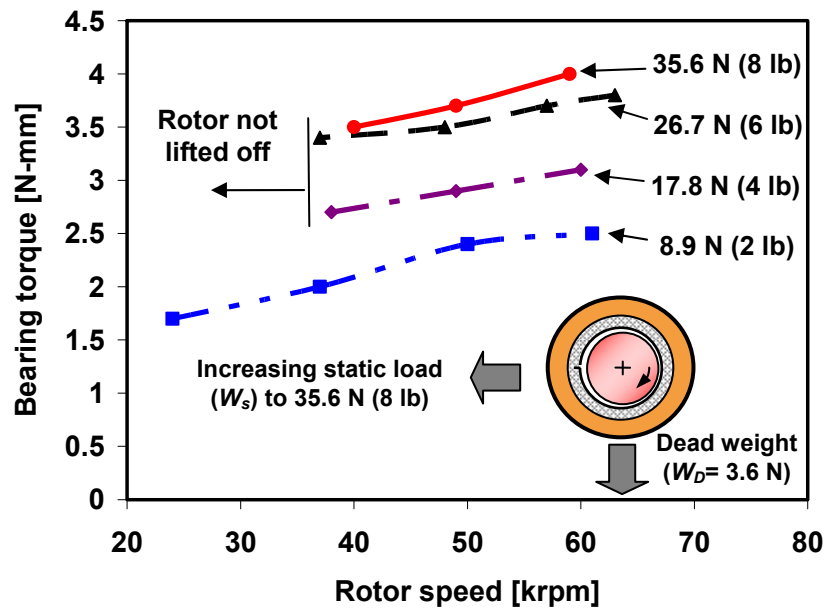
Fig. 13 Bearing viscous drag torque versus rotor speed for increasing static loads. MMFB airborne
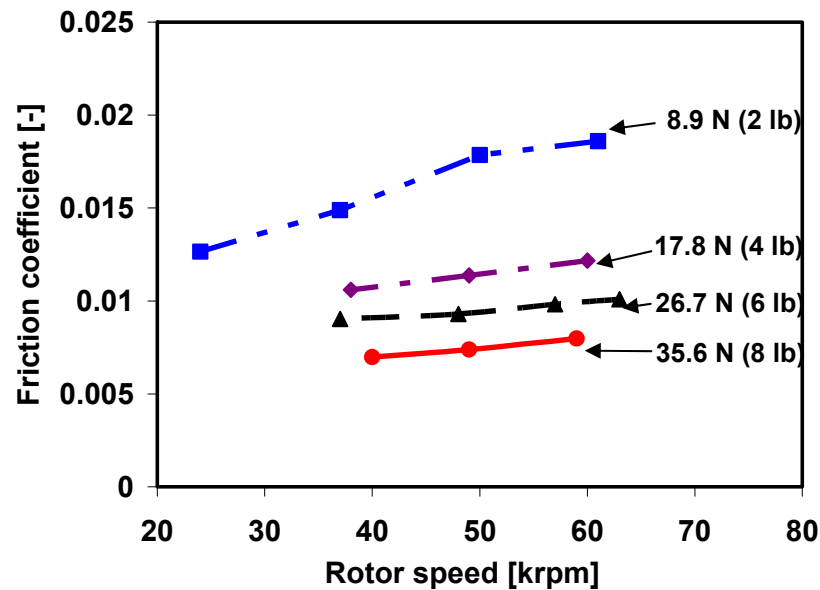
Fig. 14 MMFB friction coefficient *f* versus rotor speed for increasing static loads. Steady state operation with bearing airborne

Figure 15 displays the bearing break away torque versus static load measured during (four) rotor speed-up tests to ~ 60 krpm. The largest dry friction induced torque is observed when the rotor begins to spin. After the series of rotor liftoff tests, a post-inspection of the top foil surface showed its protective MoS_2 layer had disappeared. The top foil surface is sprayed again with the solid lubricant, and the bearing break away torque measured while rotating the journal manually. Figure 15, showing these measurements, clearly depicts that the recoated top foil surface reduces the drag torque, for instance by ~30 % for the highest static load of 35.8 N.
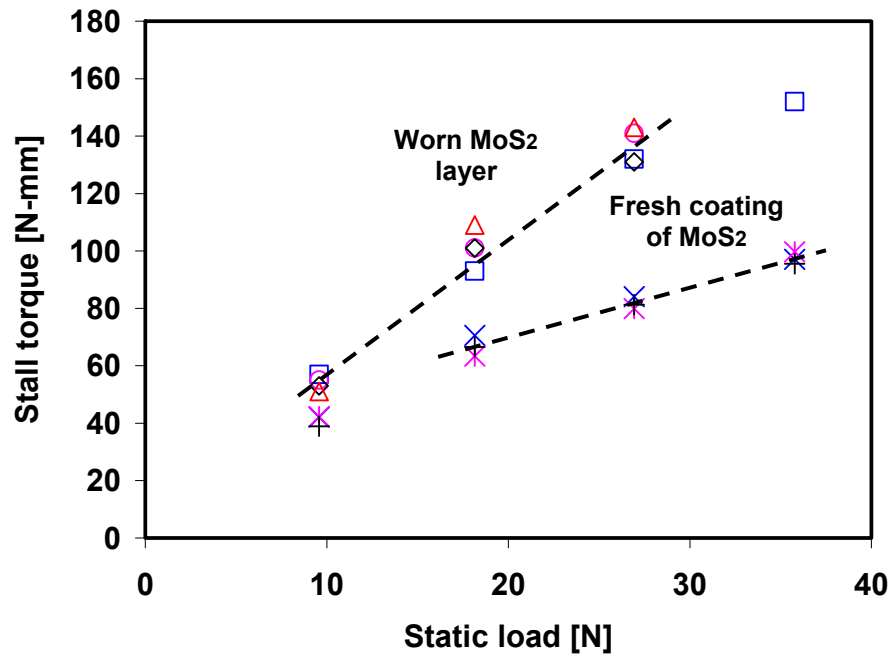
Fig. 15 MMFB break away torque versus static load. Measurements from rotor speed start up tests to 60 krpm and post-test with (fresh) MoS₂ layer deposited on top foil

Figure 16 depicts the bearing friction coefficient $f = Torque / (WR)$ estimated from the measurements shown in Figure 15. This friction coefficient represents the rubbing contact (dry frictional sliding) between the rotor and the top foil surface. The estimated value of f decreases from ~0.4 to ~ 0.37, with an increase in the static load from 9.6 N to 35.8 N, for the top foil with a worn layer of MoS_2. These friction coefficient magnitudes are typical for metal to metal contact. After spraying the top foil with a new sacrificial layer of MoS_2, the dry friction coefficient ranges from ~0.3 to 0.2 as the static load increases from 9.6 N to 35.8 N. The experimental results imply the need of adequate and enduring solid lubricants to reduce MMFB drag torque during the rotor start up (and shut down.
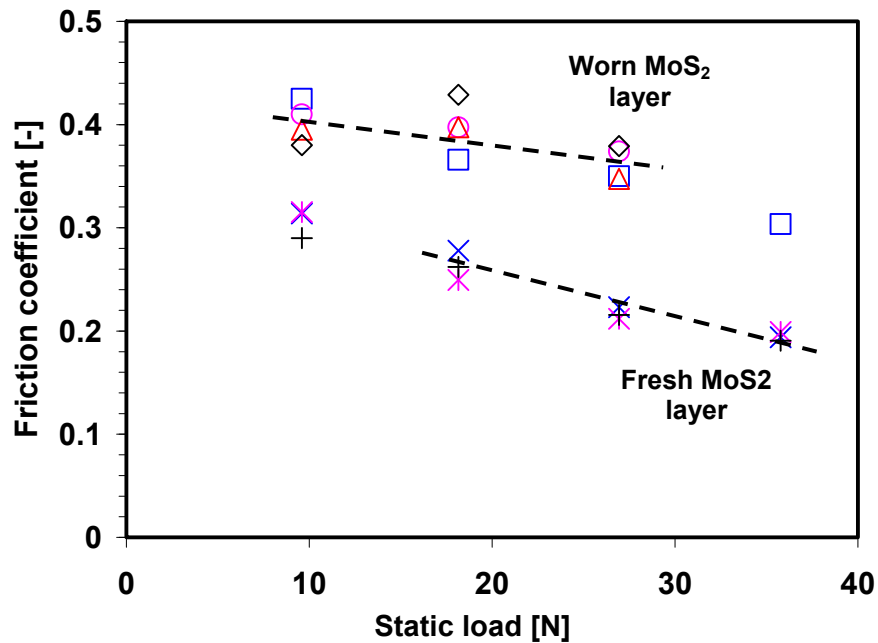
Fig. 16 Dry-friction coefficient of MMFB versus static loads. Measurements from rotor speed start up tests to 60 krpm and post-test with (fresh) MoS$_2$ layer deposited on top foil

Figure 17 shows the bearing drag torque versus rotor speed, during rotor speedup, for increasing static loads of 9.6 N, 18.2 N, 26.9 N and 35.8 N. Note that the uncertainty in drag torque is ± 0.35N-mm for drag torque < 10 N-mm. For each static load, as the rotor speed increases, initially the bearing drag torque decreases quickly and, when the journal is airborne, increases gradually with rotor speed. The lowest drag torque provides the rotor lift off speed. Note that for operation at 60 krpm, the measured drag torque is nearly identical to those recorded under steady journal speed, see Figure 13. Figure 18 show that the friction coefficient f changes only slightly with rotor speed after the rotor is airborne, i.e. once the MMFB operates with a hydrodynamic film. The identified f is the lowest for the largest applied load of 35.8 N.

Owing to the very low friction coefficient, f ~0.01 to 0.02 (when the bearing is airborne), the drag power losses in the bearing are rather small. For example, at 60 krpm

and the highest static load, the estimated power loss, $P=T_{orque}$ x $\Omega \sim 4$ N-mm x 60000 $(\pi/30) = 25.1$ W.

The rotor lift-off speed, as shown in Figure 19, is proportional to the static load imposed on the bearing. Once the shaft starts spinning, the bearing drag torque rises to a peak; then at a certain threshold speed when the bearing is airborne, the torque suddenly drops and remains at this small magnitude as long as there is an air film. The rotational speed beyond which the bearing operates with a significantly smaller drag torque, in comparison to the large startup rubbing torque, is herby termed the lift off speed, as shown in Figure 17. Note that the rotor lift-off speed also indicates the lowest rotor speed to support a static load without rubbing or contact between the shaft and top foil. Please see Appendix B for an uncertainty analysis of the torque measurements.
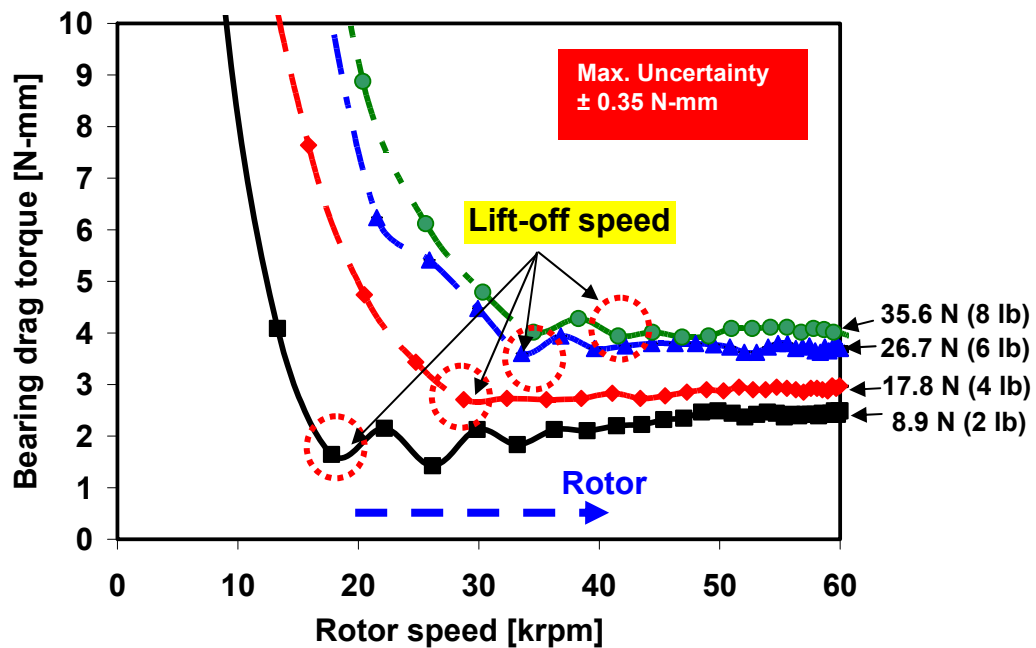
Fig. 17 Bearing drag torque versus rotor speed for increasing static loads. Measurement during rotor speed-up tests
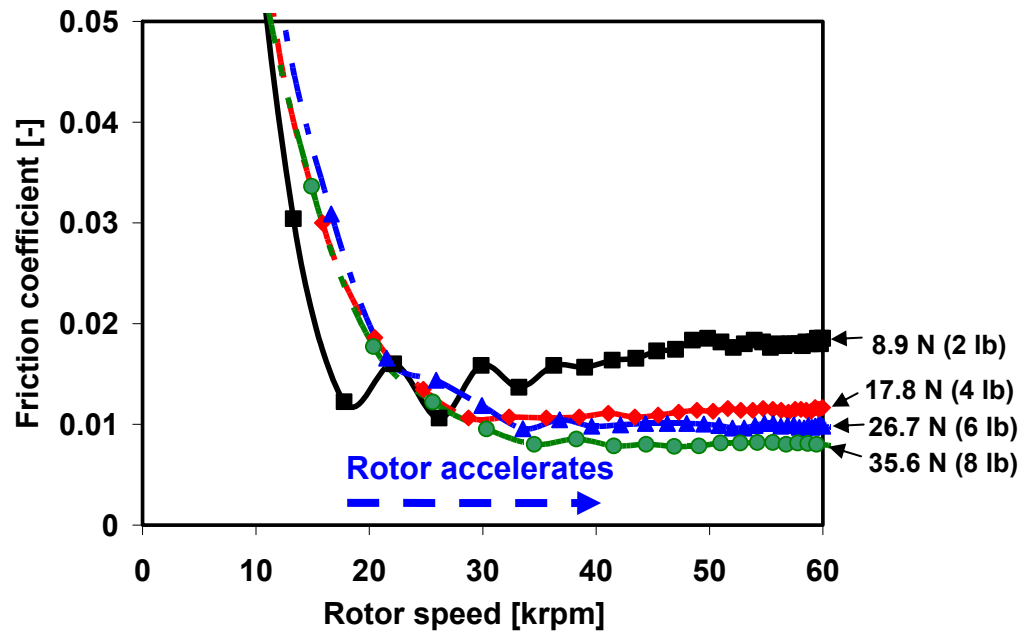
Fig. 18 Friction coefficient versus rotor speed for increasing static loads. Measurement during rotor speed-up tests
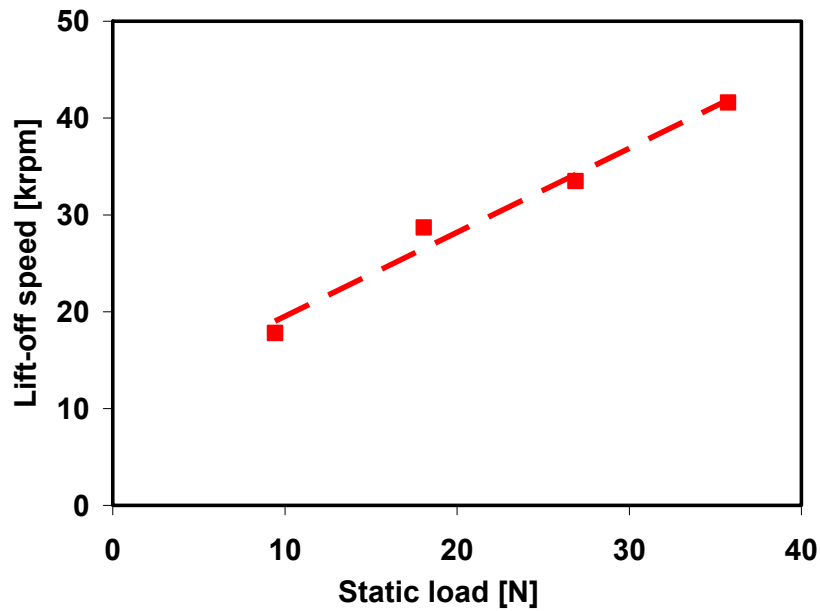
Fig. 19 MMFB: Rotor lift-off speed versus static load from smallest drag torque (see Fig.17)

MEASUREMENT OF TOP FOIL TEMPERATURE

Figure 20 shows the bearing temperature rise versus rotor speed for increasing static loads. The temperature is measured at the free end of the bearing with a thermocouple glued on the back surface of the top foil. The temperatures shown correspond to steady state values after continuous operation, no less than15 minutes, at the specified load and rotor speed. The elapsed time for the entire test is four hours. In general, the bearing temperature increases linearly with rotor speed and applied static load, as also reported in Ref. [30]. At the two lowest rotor speeds, the measured temperatures are identical uncertainty ± 0.5 °C). In general, the temperature increase is quite modest for the test since the specific loads applied are rather small, i.e. W_{max}/LD= 45.5 kN/m^2 (6.6 psi).
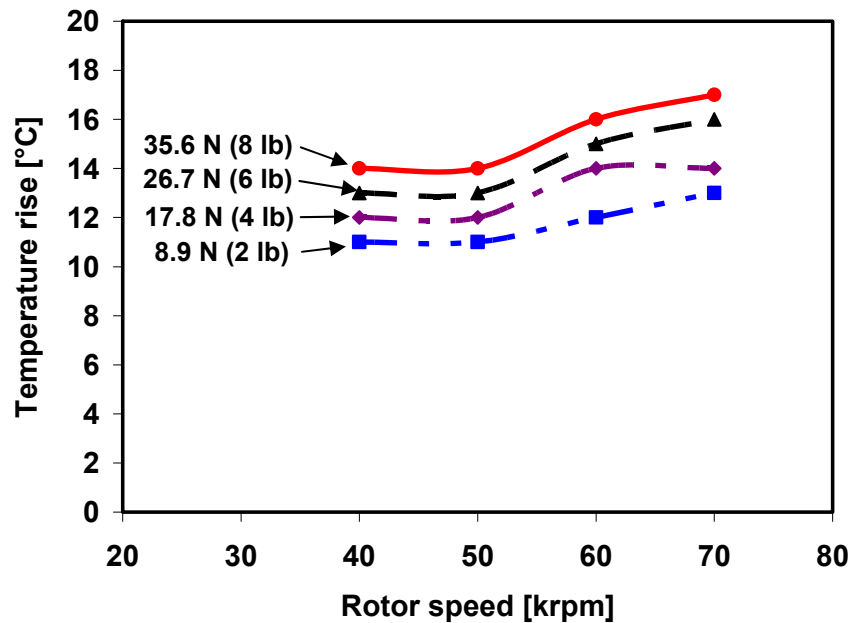
Fig. 20 Bearing temperature rise versus rotor speed for airborne operation with increasing static loads. Estimation at steady state rotor speeds (after 15 min. for each condition). Ambient temperature at 21 °C

CHAPTER V

IDENTIFICATION OF MMFB STIFFNESS AND DAMPING COEFFICIENTS FROM IMPACT LOAD TESTS

MODEL OF THE TEST BEARING

Figure 21 shows a representation of the bearing force coefficients and the impact forces exerted on the test bearing. Recall that the bearing floats atop the rotating shaft or journal, and it rests on the journal while the journal is not rotating.
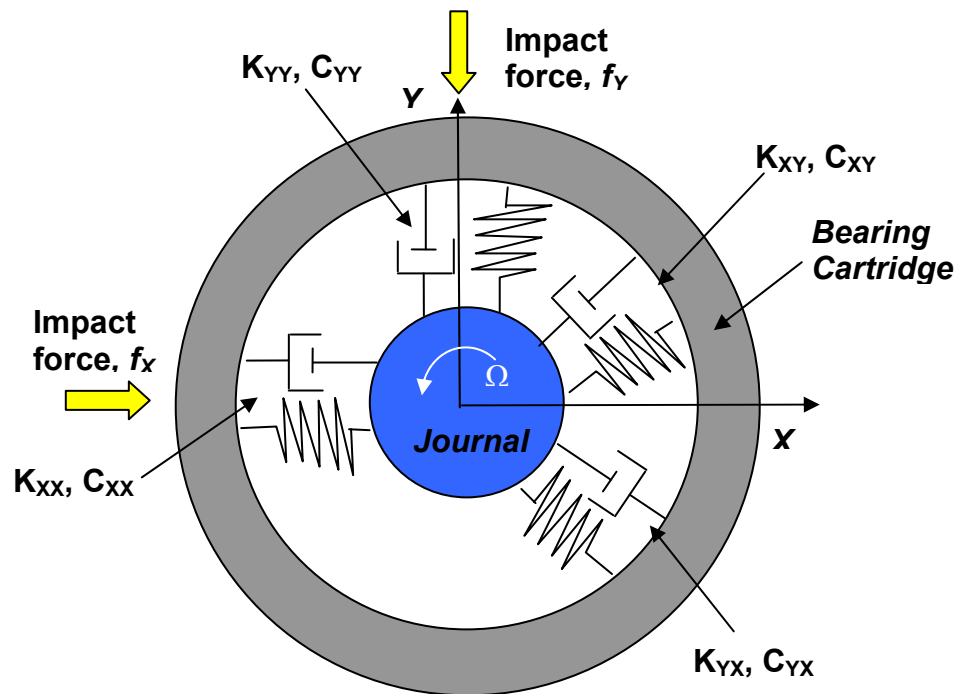
Fig. 21 Representation of bearing force coefficients and impact forces acting on test bearing

The equations of motion of the test bearing modeled as a 2DOF mechanical system are

$$\begin{pmatrix} f_X - M\,a_X \\ f_Y - M\,a_Y \end{pmatrix} = \begin{bmatrix} C_{XX} & C_{XY} \\ C_{YX} & C_{YY} \end{bmatrix} \begin{pmatrix} \delta\dot{x} \\ \delta\dot{y} \end{pmatrix} + \begin{bmatrix} K_{XX} & K_{XY} \\ K_{YX} & K_{YY} \end{bmatrix} \begin{pmatrix} \delta x \\ \delta y \end{pmatrix} \tag{1}$$

where $\{f_i\}_{i=X,Y}$ are the excitation forces, $M=0.38$ kg is the test system mass, $\{a_i\}_{i=X,Y}$ are the accelerations of the bearing cartridge, and $\{K_{ij}, C_{ij}\}_{i,j=X,Y}$ are the bearing stiffness and damping coefficients, respectively. δX and δY are the relative displacements of the bearing with respect to the journal in the horizontal and vertical directions.

Only one of the equations above is needed to identify the stiffness and damping coefficients when the journal does not spin. This is so since cross coupled coefficients are nil without journal rotation. Thus, the uncoupled equation of motion along one direction (Y) represented in the frequency domain is

$$\frac{F_Y}{Y} = \left[K_{YY} + M^*(A_Y/Y) \right] + \left[i\omega C_{YY} \right] \tag{2}$$

where F_Y, A_Y and Y are the FFTs of the impact force, the bearing accelerations and the relative bearing displacement along the vertical (y) direction. $K_{XX} = K_{YY}$ and $C_{XX} = C_{YY}$ are the identified bearing stiffness and equivalent viscous damping coefficients, and ω is the excitation frequency.

TEST CONFIGURATION

Figure 22 illustrates the schematic view of the test configuration for identifying the bearing stiffness and damping coefficients along the vertical direction with impact load tests. An eddy current sensor, at one end of the bearing cartridge, measures the bearing displacement with respect to the journal. The model assumes that the whole bearing cartridge remains parallel to the journal. A miniature accelerometer (5.1 g) records the accelerations of the bearing cartridge. Ten impacts are provided in the vertical direction. Frequency domain averages are used to estimate the bearing force coefficients.
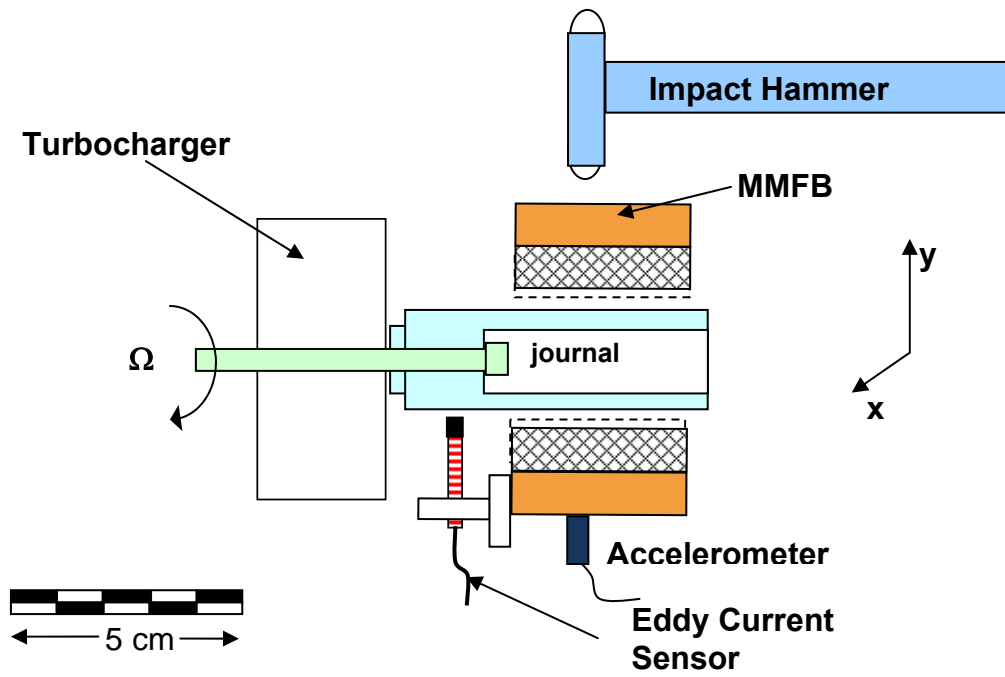
Fig. 22 Schematic view representing the impact loading of MMFB

IMPACT LOAD TEST RESULTS (SHAFT NOT ROTATING)

Figures 23 and 24 show the impact force applied at the bearing midspan and along the vertical direction, in the time and frequency domains, respectively. Ten impact loads are applied; the motion responses are recorded and averaged in the frequency domain. Note that the bearing rests on the non rotating shaft. The bearing weight is the only static load acting on the MMFB.
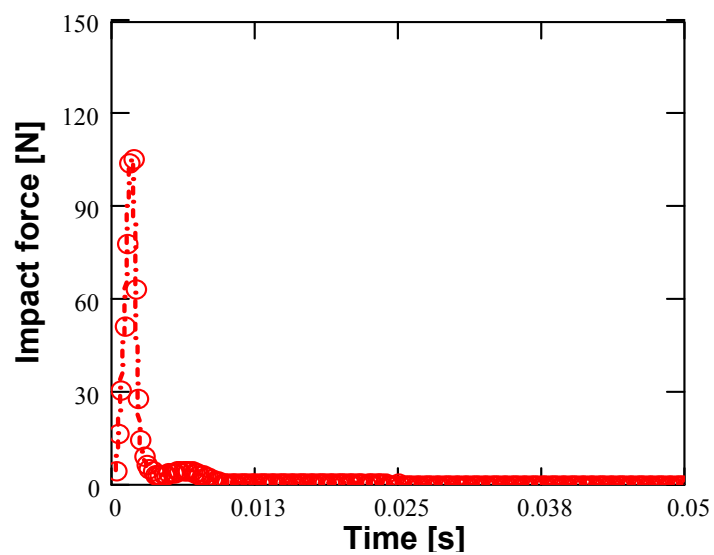
Fig. 23 Typical impact force along vertical direction
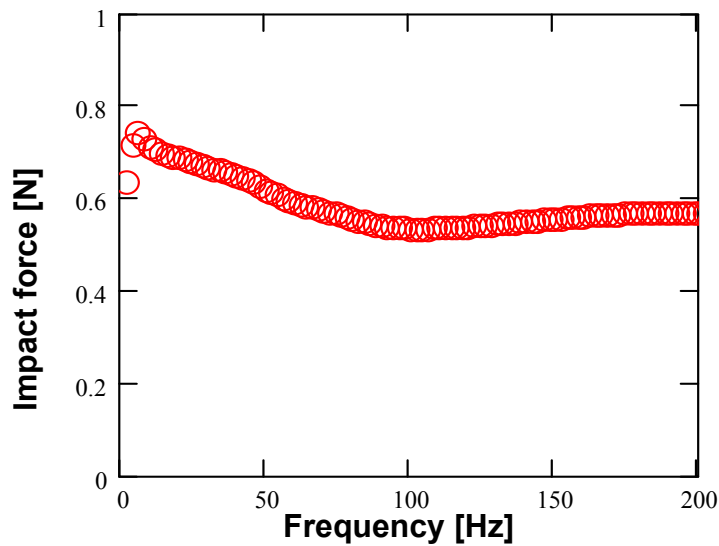
Fig. 24 FFT amplitude of impact force along vertical direction. Average of 10 impacts

Figures 25 and 26 show the bearing displacements relative to the shaft, in time and frequency domains respectively. Note how the displacement amplitudes decrease rapidly with time, i.e. the test bearing appears to have large damping. Figure 27 shows, for frequencies up to 200 Hz, an excellent coherence (~ 1.00) for the bearing displacements due to 10 impact loads. The coherence between the signals is rather poor at higher frequencies (> 200 Hz) as the impact force clearly does not excite high frequency components.
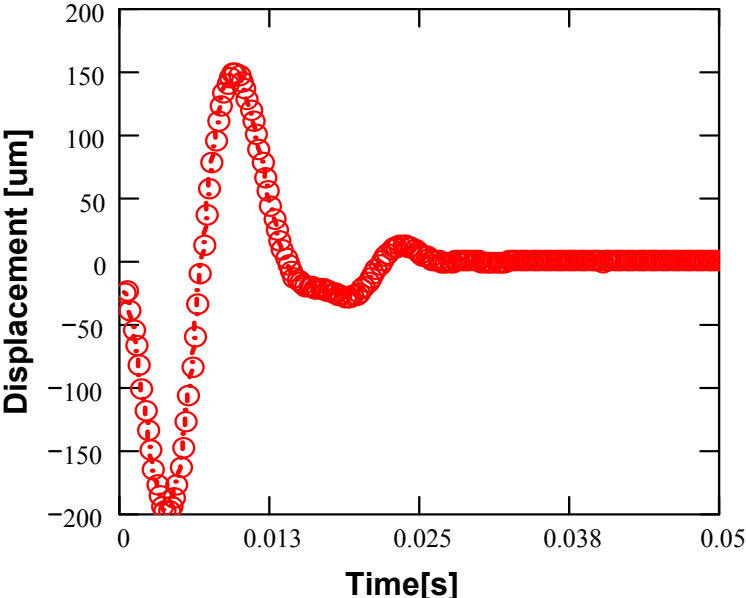
Fig. 25 Typical bearing *Y* displacement with respect to shaft versus time. Motion due to an impact force along vertical direction. Journal not rotating
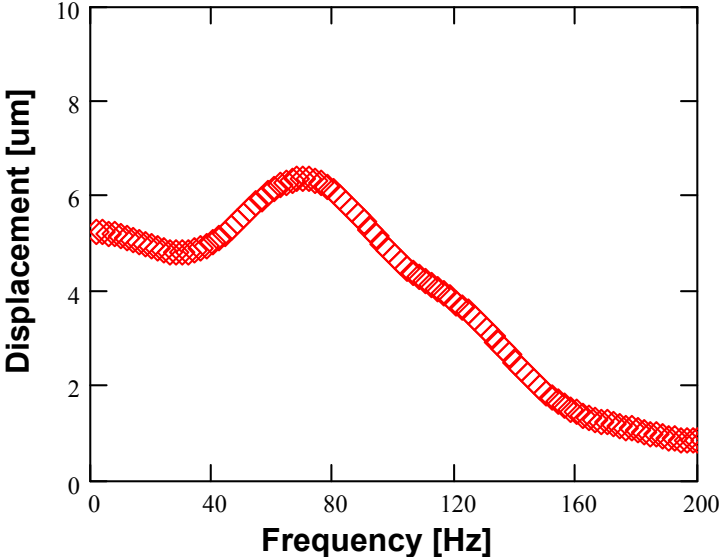
Fig. 26 FFT amplitude of bearing *Y* displacement with respect to shaft due to an impact force along vertical direction. Average of 10 impacts. Journal not rotating
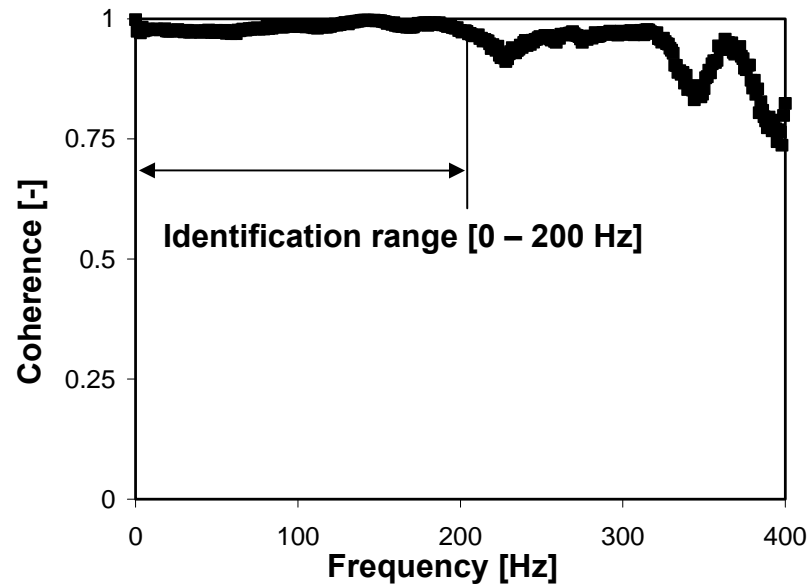
Fig. 27 Coherence between impact force and *Y* direction displacement signal. Average of 10 impacts. Journal not rotating

Figure 28 depicts the FFT of the bearing cartridge acceleration (A_Y) and the acceleration $|-\omega^2 Y|$ derived from the relative displacement of the MMFB and its journal. The two accelerations must coincide if the journal does not move. Alas, this is not the case since the shaft stub of the turbocharger is rather flexible. Hence, the cartridge acceleration must be kept, as measured, in the model for identifying the stiffness and damping coefficients, see Eq. (C2). Substituting $A_Y = -\omega^2 Y$ is not correct.

The bearing model, see Eqn. (2), includes three unknowns, the bearing structural stiffness (K_{YY}), the equivalent viscous damping (C_{YY}), and the bearing mass (*M)*. Figure 29 shows a curve fit of the test data identifying the bearing *static* structural stiffness[3] K_{YYo} = 0.23 MN/m and system mass *M*=0.381 kg, which is nearly identical to the measured mass of 0.380 kg.

---

[3] Frequency independent stiffness
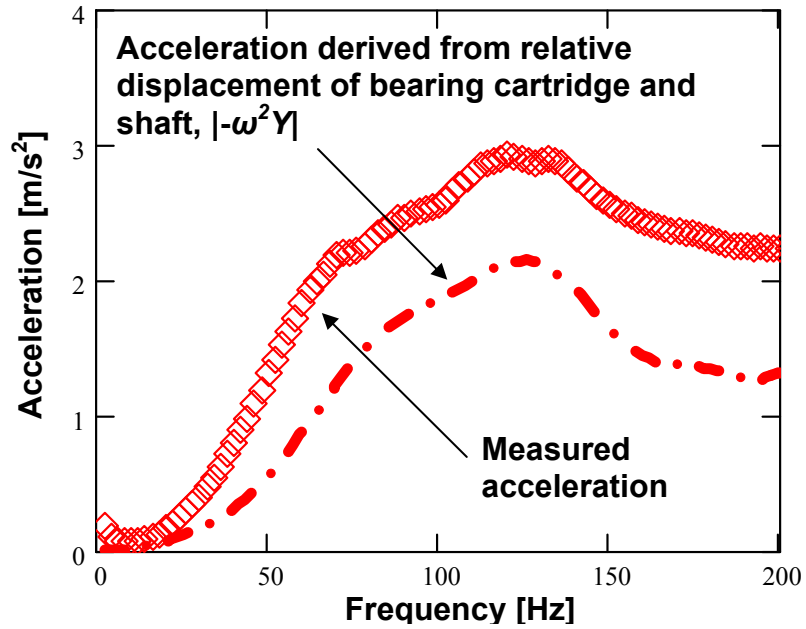
Fig. 28 FFT amplitudes of acceleration of bearing cartridge (measured and derived from displacement) versus frequency. Average of 10 impacts. Journal not rotating
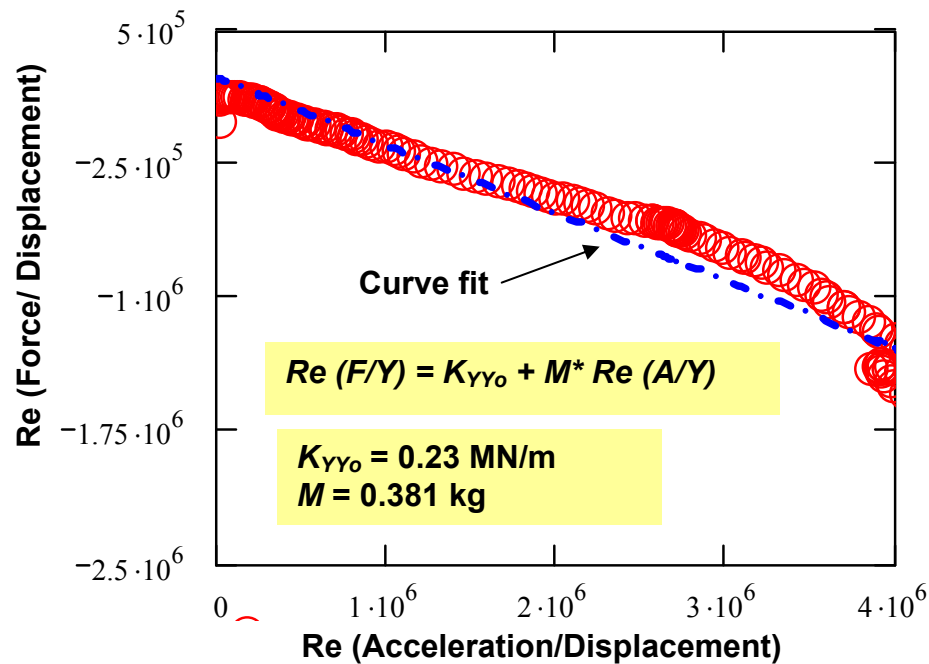
Fig. 29 (Force/displacement) versus (acceleration/displacement), and linear fit identifying the MMFB structural stiffness and mass coefficients. Average of 10 impacts. Journal not rotating

The estimated test system natural frequency is $f_n = (K_{YYo}/M)^{0.5} = 123$ Hz, and the system critical damping $C_{crit} = 2*(K_{YYo}M)^{0.5} = 592$ N.s/m. Note that the amplitude of the bearing cartridge acceleration is the highest around the identified system natural frequency of ~ 123 Hz.

The MMFB structural stiffness in actuality changes with frequency [6]. Hence a frequency dependent stiffness coefficient $K_{YY}(\omega)$ is identified for frequencies up to 200 Hz using eqn. (2) and a fixed mass of M = 0.38 kg. Figure 30 shows the identified bearing structural stiffness K_{YY} increasing with frequency. The structural stiffness is ~ 0.15 MN/m at 0 Hz, and increases to ~ 0.4 MN/m at 200 Hz. Note that the structural stiffness is inversely proportional to the bearing displacement [6]. Figure 31 depicts the estimated equivalent viscous damping C_{YY} decreasing from ~ 420 Ns/m to ~100 Ns/m as the frequency increases from 0 to 200 Hz. The damping ratio (C_{YY}/C_{crit}) decreases from ~

0.7 to 0.17. In general, the viscous damping in a metal mesh structure is inversely proportional to the frequency and amplitude of motion.

Prior estimation of the bearing structural stiffness and equivalent viscous damping coefficient, using unidirectional single frequency loads [6], shows a larger stiffness and damping coefficient (>3 times), see Figures 3 and 4. Note that a shaft different from that reported in Ref. [6] is used in the current experiments. The clearance in the MMFB-shaft assembly is presently larger[4]. The metal mesh ring static structural stiffness increases nonlinearly with displacement amplitude. Also, note that bearing creep or sag over time may result in the reduction in magnitude of the force coefficients [6].

The uncertainty of the identified force coefficient is due to the uncertainties propagated from individual measurements of force (< 2%), acceleration (< 1%) and bearing displacement (< 0.2%). The uncertainty in stiffness and damping coefficients is <5 % of their identified magnitude for frequencies above 50 Hz up to 200 Hz. However, below 50 Hz the uncertainty associated with the equivalent viscous damping coefficient is greater than 5 % due to the uncertainty in frequency (± 1 Hz).For repeatability of the identified coefficients, see Appendix D.

---

[4] The top foil and the shaft are in contact upon assembly. Hence, the concept of nominal clearance in a foil bearing is rather vague [25]

$$K_{YY} = Re \{(F - MA_y)/Y\}$$

$$K_{YYo} = 0.23 \text{ MN/m}$$
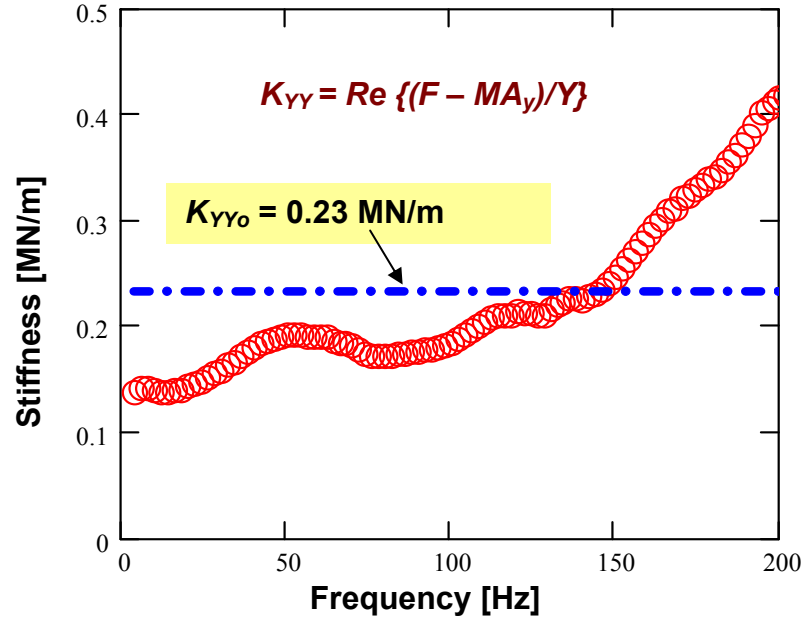
Fig. 30 Identified MMFB structural stiffness K_{YY} versus frequency. Journal not rotating

$$C_{YY} = Im \left[\frac{(F - M_{est} A_y)/Y}{\omega} \right]$$
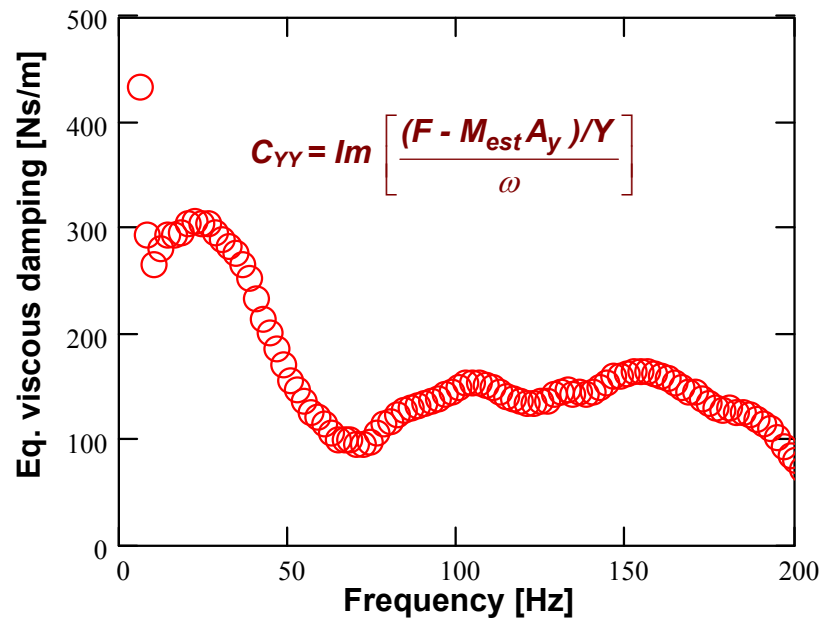
Fig. 31 Identified MMFB equivalent viscous damping C_{YY} versus frequency. Journal not rotating

IMPACT LOAD TEST RESULTS (SHAFT ROTATING AT 50 KRPM)

Prior to conducting impact load tests, the baseline motion of the MMFB relative to the rotating shaft spinning at 50 krpm is recorded. The bearing weight of 3.5 N and a pull load of 3.5 N along the horizontal direction are the only static loads acting on the MMFB. Within the frequency range 0 – 1000 Hz, Figure 32 shows that, without an impact load, the FFT amplitudes of relative bearing displacements along X and Y directions are less than 0.5 μm except at the synchronous $1X$ and subsynchronous $\frac{1}{2}X$ frequencies. Most importantly, the bearing displacements are ~ 2μm around 830 Hz (50 krpm) and ~ 1μm around 410 Hz (~ $\frac{1}{2}X$).

Large subsynchronous motions are present when the bearing is lightly loaded, for instance with a static load of 3.5 N along the horizontal direction. Although, a "half-frequency" whirl may lead to instability, the rotor-bearing system remains stable up to a speed of 60krpm (1000 Hz) even with a light load of 3.5 N. Operation at higher rotor speeds was not attempted.

In Appendix C, full spectrum cascade plots of the orbits of bearing displacements relative to the rotating shaft show that, as the applied pull load increases, the $\frac{1}{2}X$ components of the bearing displacements vanish at frequencies above 40 krpm. However, with an increasing load, the displacement amplitudes around the rotor natural frequencies become significant.

Figures 33 and 34 show the impact force, acting along the vertical direction at the bearing midspan, in both time and frequency domains, respectively. The shaft rotates at 50 krpm (834 Hz) and the MMFB floats on the rotating shaft; i.e., bearing is airborne. The bearing weight of 3.5 N and a pull load of 3.5 N along the horizontal direction are the only static loads acting on the MMFB.
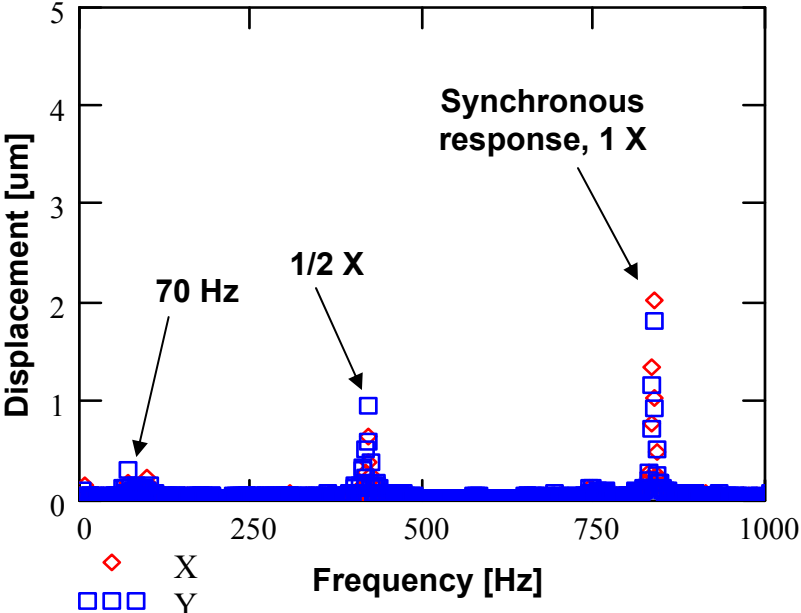
Fig. 32 FFT amplitudes of bearing displacements with respect to the shaft. Baseline response. Applied static load of 3.5 N in horizontal direction. Bearing weight of 3.5 N. Average of 10 responses. Journal rotating at 50 krpm (834 Hz)
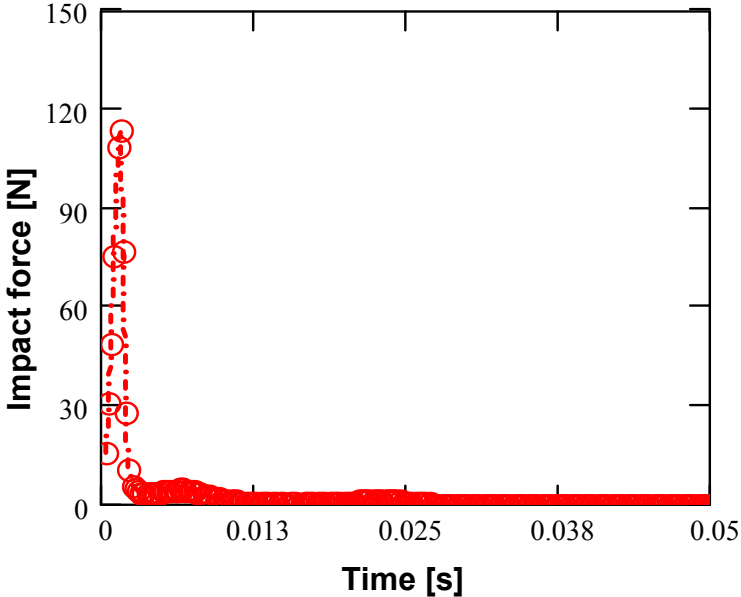
Fig. 33 Typical impact force along vertical direction (*Y*) versus time
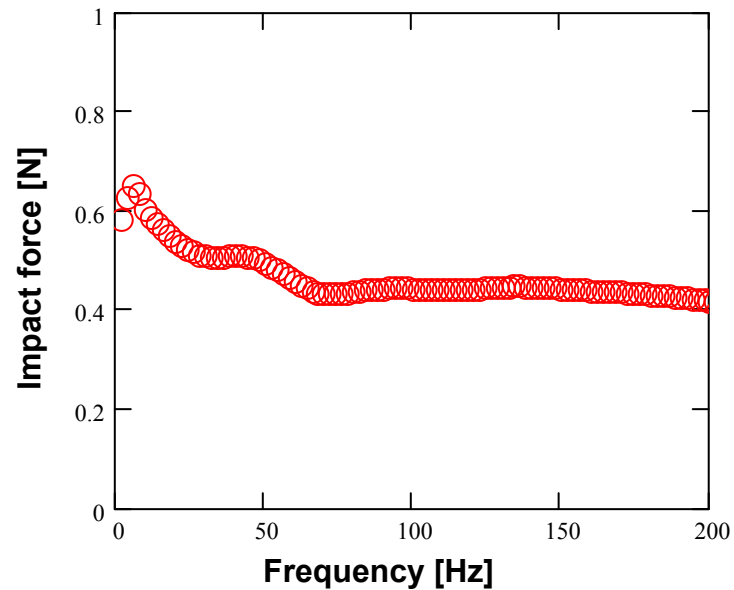
Fig. 34 FFT amplitude of impact force along vertical direction (*Y*). Average of 10 impacts

Figures 35 and 36 depict the measured bearing displacements, relative to the rotating journal, in both time and frequency domains, respectively. Even without an impact force, because of the spinning rotor, the FFT amplitudes of relative bearing displacements show vibration amplitudes with frequencies above 200 Hz, see Figure 32. Hence, higher frequency components (>200 Hz) are filtered to evidence the response due to the impact force alone. The filtered displacement amplitudes show that the bearing motion is underdamped, the displacements setling down in ~0.05 second.
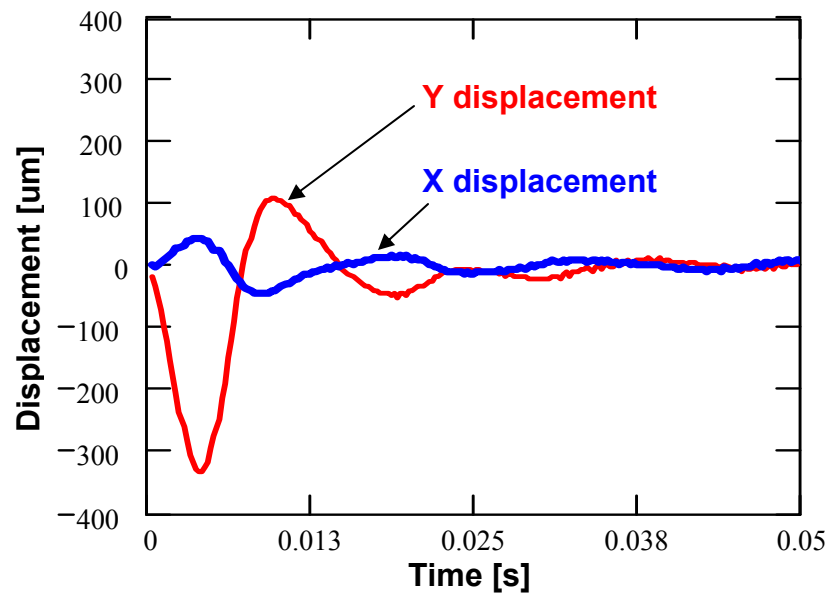
Fig. 35 Typical bearing displacements with respect to shaft due to an impact force along vertical direction (*Y*). Time domain data shows the bearing response to one of ten impact loads. Higher frequency components (> 200 Hz) filtered. Applied static load of 3.5 N in horizontal direction. Bearing weight of 3.5 N. Journal rotating at 50 krpm (834 Hz)
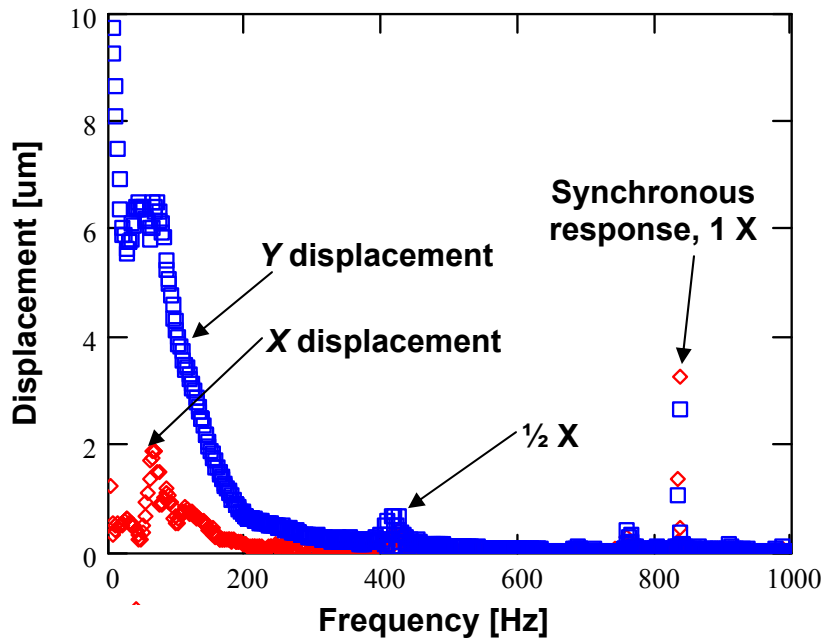
Fig. 36 FFT amplitude of bearing displacements with respect to the shaft due to the impact force along vertical direction (*Y*). Average of 10 impacts. Applied static load of 3.5 N in horizontal direction. Bearing weight of 3.5 N. Journal rotating at 50 krpm (834 Hz)

Figure 37 shows the coherence between the impact force and the relative bearing displacements along vertical and horizontal directions for frequencies up to 800 Hz. The coherence of the *Y* displacement is excellent up to a frequency of 200 Hz. However, the coherence of the *X* displacement is above 0.8 only over a small frequency range, 50 -150 Hz, because of noise affecting the *X* displacement, relatively smaller than the *Y* displacement. The low coherence between the *X* displacements and the impact force affects the reliability of the estimated cross coupled force coefficients. The impact force does not excite any bearing motion amplitude above 200 Hz. Hence, the parameter identification is limited to 200 Hz.

Figure 38 shows the bearing accelerations, measured and derived from relative bearing displacements, along two orthogonal directions. The accelerations derived from the relative bearing displacements are not identical to the measured accelerations since the flexible shaft can move independent of MMFB motion.
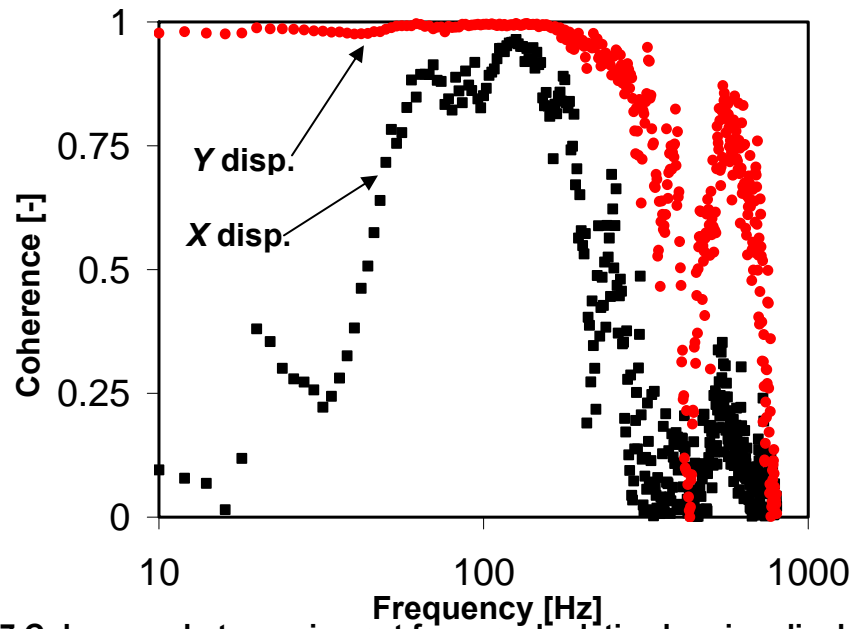
Fig. 37 Coherence between impact force and relative bearing displacement signals versus frequency. Average of 10 impacts. Applied static load of 3.5 N in horizontal direction (*X*). Bearing weight of 3.5 N. Journal rotating at 50 krpm (834 Hz)

**Fig. 38 FFT amplitude of acceleration of bearing cartridge (measured and derived from displacement) versus frequency. Average of 10 impacts. Applied static load of 3.5 N in horizontal direction(*X*). Bearing weight of 3.5 N. Journal rotating at 50 krpm (834 Hz)**

For small static loads, it is reasonable [31] to assume that $K_{XX} = K_{YY} = K$, $K_{XY} = -K_{YX} = k$, $C_{XX} = C_{YY} = C$ and $C_{XY} = -C_{YX} = c$. The stiffness and damping coefficients are readily identified from the algebraic equations

$$K = K_{XX} = K_{YY} = Re\left[\frac{(F_Y - M \cdot A_Y)Y + (M \cdot A_X)X)}{X^2 + Y^2}\right]$$

$$k = K_{XY} = -K_{YX} = Re\left[\frac{(-M \cdot A_X) \cdot Y - (F_Y - M \cdot A_Y) \cdot X}{X^2 + Y^2}\right]$$

$$C = C_{XX} = C_{YY} = Im\left[\frac{(F_Y - M \cdot A_Y)Y + (M \cdot A_X)X)}{X^2 + Y^2}\right] \cdot \left(\frac{1}{\omega}\right)$$ (3)

$$c = C_{XY} = -C_{YX} = Im\left[\frac{(-M \cdot A_X) \cdot Y - (F_Y - M \cdot A_Y) \cdot X}{X^2 + Y^2}\right]\left(\frac{1}{\omega}\right)$$

where ω is the excitation frequency and F_Y, A_X, A_Y and X, Y are the FFTs of the impact force, the bearing accelerations and the relative bearing displacements. $K_{XX} = K_{YY} = K$ and $C_{XX} = C_{YY} = C$ are the identified bearing direct stiffness and direct equivalent viscous damping coefficients. The bearing mass $M = 0.38$ kg is a fixed parameter.

Figure 39 shows that the identified bearing direct stiffness ($K = K_{XX} = K_{YY}$) gradually increases from 0.07 MN/m at 0 Hz to 0.3 MN/m at 200 Hz. The test results indicate that the cross coupled stiffnesses are of the same order of magnitude as the direct stiffness. Figure 40 depicts the estimated direct equivalent viscous damping ($C = C_{XX} = C_{YY}$), decreasing from ~ 500 Ns/m to ~ 100 Ns/m as the frequency increases from 0 to 200 Hz. The stiffness and damping coefficients follow trends similar to one obtained from experiments without shaft rotation. However, the identified stiffness is lower, ~ 30 % at 100 Hz and ~ 25 % at 200 Hz, when the bearing is airborne. The equivalent viscous damping coefficient is almost similar in value to that identified without shaft rotation.

The structural damping in the MMFB comes from the metal mesh ring installed beneath the top foil. The material damping property of the metal mesh ring is best represented with a loss factor ($\gamma = C\omega/K$) defined as the ratio of the product of the direct equivalent viscous damping coefficient and excitation frequency to the bearing stiffness. Figure 41 shows the identified loss factors, with and without shaft rotation, versus frequency. While rotating at 50krpm, the estimated loss factor is ~ 0.5, a large magnitude for the simple mechanical system. Prior experiments, with unidirectional single frequency loads, show a loss factor of ~ 0.7 for the same bearing [6]. However, for the low frequency range (0-125 Hz), the loss factor identified from tests without rotation is lower than that determined from tests with the journal rotating at 50 krpm. At higher frequencies (> 125 Hz), both loss factors are nearly identical.
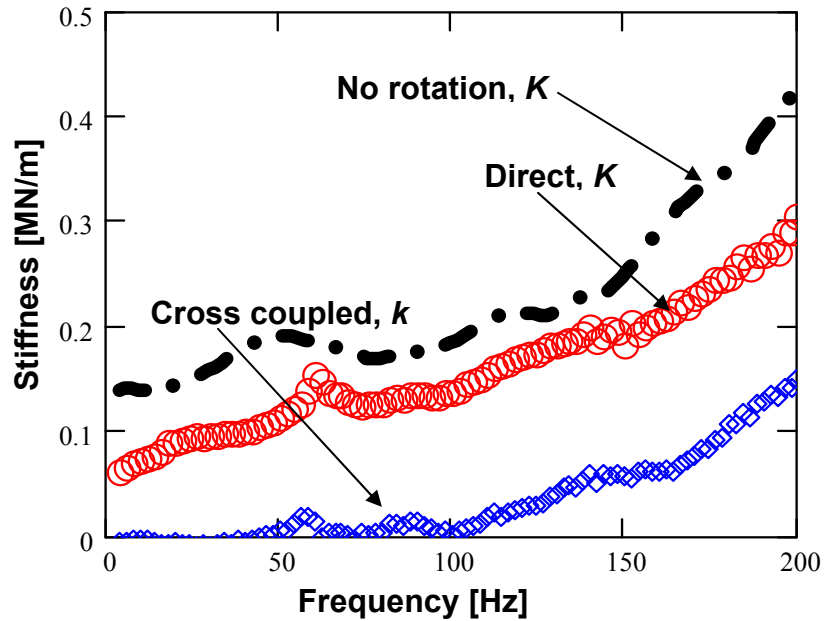
Fig. 39 Identified MMFB direct (*K*) and cross coupled (*k*) stiffnesses versus frequency. Applied static load of 3.5 N in horizontal direction (*X*). Bearing weight of 3.5 N. Journal rotating at 50 krpm (834 Hz)
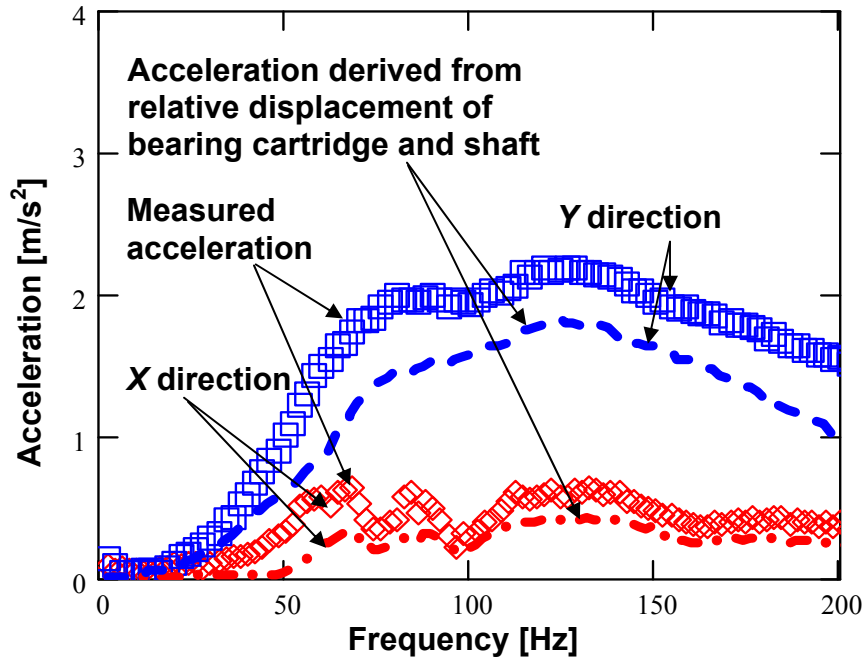

Fig. 40 Identified MMFB direct (*C*) and cross coupled (*c*) equivalent viscous damping coefficients versus frequency. Applied static load of 3.5 N in horizontal direction (*X*). Bearing weight of 3.5 N. Journal rotating at 50 krpm (834 Hz)

Fig. 41 Identified MMFB loss factor (γ) versus frequency. Applied static load of 3.5 N in horizontal direction (*X*). Bearing weight of 3.5 N. Journal rotating at 50 krpm (834 Hz)
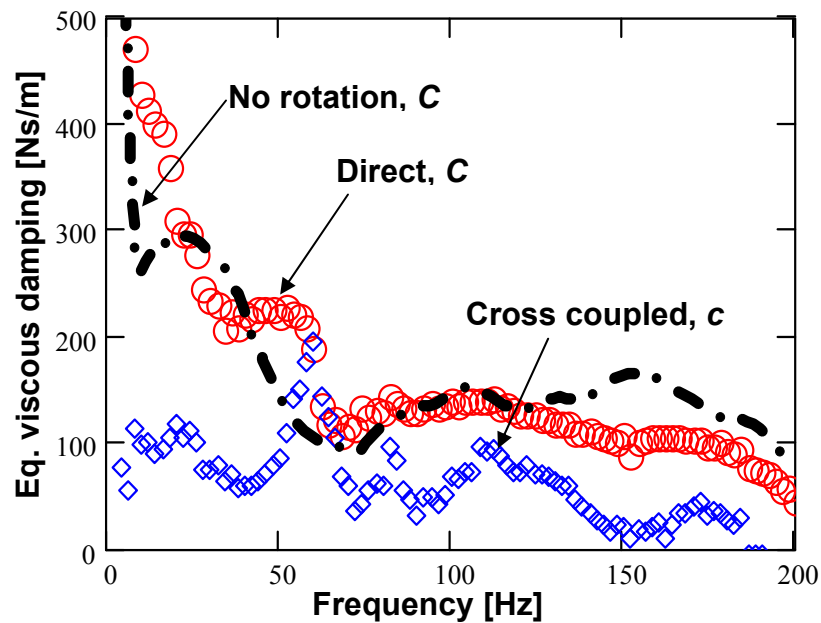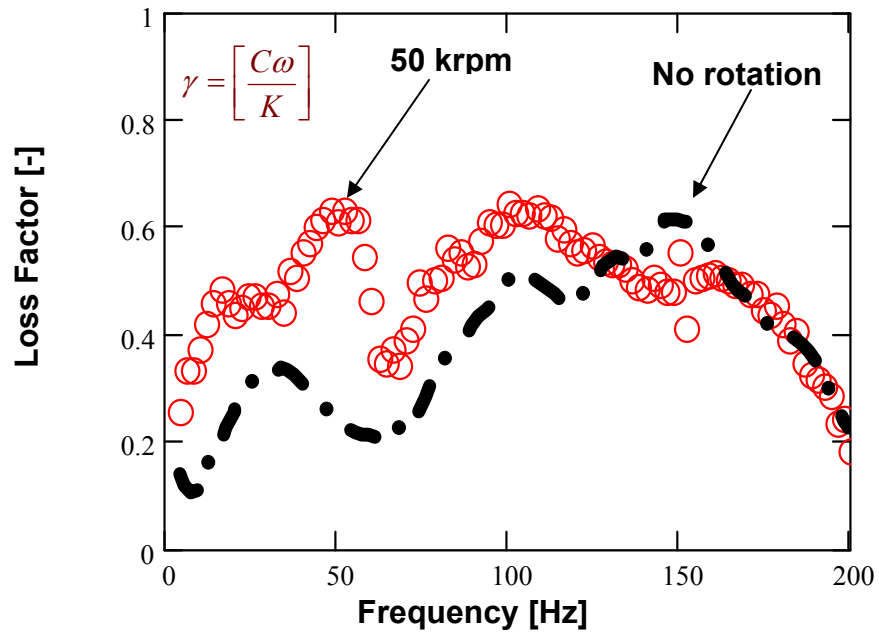
CHAPTER VI
CONCLUSIONS

Metal mesh foil bearings (MMFBs) offer promise as a reliable support in oil-free high speed rotating machinery. MMFBs provide a tunable resilient support with large (material) damping. Most importantly, the MMFB configuration is simple and of little cost since it uses commercially available materials. Note that metal mesh ring structural properties can be changed by modifying its geometrical dimensions and compactness, thus promoting the scalability of this bearing technology.

The thesis presents the measurement of drag torque, rotor lift-off speed, and operating temperature of a test MMFB mounted on a turbocharger air turbine driven test rig. The measurements aim to characterize the static load performance of the MMFB over broad ranges of rotor speed and static loads. The measurements show that the bearing break-away torque during rotor speed start-up increases with increasing static loads. This break-away torque, typical of dry friction contact, is reduced by application of a sacrificial layer of MoS_2. During rotor airborne (hydrodynamic) operation, the bearing drag torque increases with the static load and rotor speed. However, the friction coefficient is rather small (< 0.010) denoting negligible power losses. The rotor lift-off speed, estimated at the lowest drag torque, increases linearly with static load. The test bearing steady state temperature is proportional to rotor speed and increases with the applied static load.

MMFB structural stiffness and damping coefficients are identified, for the range of frequencies 0-200 Hz, from impact load tests while i) the shaft is at rest and ii) the shaft runs at 50 krpm (834 Hz). The only load is due to the bearing weight when an impact test is conducted without shaft rotation. The bearing response shows a system with large damping. The frequency dependent stiffness increases from ~0.15 MN/m at 0 Hz to ~0.4 MN/m at 200 Hz. The equivalent viscous damping coefficient decreases from ~ 420 Ns/m to ~100 Ns/m as the frequency increases up to 200 Hz. Impact load tests on the bearing and with the shaft running at 50 krpm (834 Hz) show appreciable cross

directional motions, indicating significant cross coupled stiffness and cross coupled damping while the bearing is airborne. The identified direct stiffness is smaller (~ 25% at 200 Hz) than the structural stiffness of the MMFB. The equivalent viscous damping, estimated while the shaft spins at 50 krpm, is nearly identical (within the variability) to the equivalent viscous damping estimated from impact load tests without shaft rotation. The estimated loss factor is ~ 0.5. The loss factor for the two test cases, with and without shaft rotation, is nearly identical at frequencies >125 Hz.

The orbits of bearing displacements relative to the rotating shaft show reverse precession above certain rotor speeds while operating with radial loads and large eccentricity ratio, see Appendix C. However, as the applied load increases, the onset speed of backward whirl also increases.

The experimental results provide a comprehensive database on the static load performance of the simple and low cost prototype MMFB for increasing rotor speed and temperature. The measurements demonstrate the reliable performance of a MMFB for an oil-free application and pave the way for further developments.

REFERENCES

[1] Agrawal, G., 1997, "Foil Air/Gas Bearing Technology – an Overview," ASME Paper No. 97-GT-347.

[2] Valco, M.J., and DellaCorte, C., 2002, "Emerging Oil-Free Turbomachinery Technology for Military Propulsion and Power Applications," *Proceedings Of 23rd U.S. Army Science Conference*, Orlando, FL, Dec. 2-5.

[3] Al-Khateeb, E. M., 2002, "Design, Modeling and Experimental Investigation of Wire Mesh Vibration Dampers," PhD. Thesis, Texas A&M University, College Station, TX.

[4] Lee, Y. B., Kim, C. H., Jo, J. H., and Ryu, K., 2006, "Air Foil Bearing Having a Porous Foil," International Patent No. WO 2006/043736 A1.

[5] Zarzour, M. and Vance, J., 2000, "Experimental Evaluation of a Metal Mesh Bearing Damper," ASME J. Eng. Gas Turbines Power, **122**(2), pp. 326-329.

[6] San Andrés, L., Chirathadam, T. A., and Kim, T. H., 2009, "Measurement of Structural Stiffness and Damping Coefficients in a Metal Mesh Foil Bearing," ASME Paper No. GT2009-59315.

[7] Choudhry, V., and Vance, J. M., 2005, "Design Equations for Wire Mesh Bearing Dampers in Turbomachinery," ASME Paper No. GT 2005-68641.

[8] Ao, H., Jiang, H., Wei, W., and Ulanov, A.M., 2006, "Study on the Damping Characteristics of MR Damper in Flexible Supporting of Turbo-Pump Rotor for Engine," *Proc. 1st Int. Symposium on Systems Control in Aerospace and Astronautics*, Harbin, China, Jan. 19-21, pp. 618-622.

[9] Okayasu, A., Ohta, T., Azuma, T., Fujita, T., and Aoki, H., 1990, "Vibration Problems in the LE-7 Liquid Hydrogen Turbopump," AIAA Paper No. AIAA-1990-2250.

[10] Al-Khateeb, E. M., and Vance, J. M., 2001, "Experimental Evaluation of a Metal Mesh Bearing Damper in Parallel with a Structural Support," ASME Paper No. 2001-GT-0247.

[11] Ertas, B. H., Al-Khateeb, E. M., and Vance, J. M., 2003, "Rotordynamic Bearing Dampers for Cryogenic Rocket Engine Turbopumps," AIAA J. Propul. Power, **119**(4), pp. 674-682.

[12] Burshid, S.M., 1990, "Experimental Evaluation of Rotordynamic Coefficients for Hybrid Metal Mesh Pocket Damper Seals in Turbomachinery," M.S. Thesis, Texas A&M University, College Station, TX.

[13] Ashrafi, S.A., and Smyth, A.W., 2007, "Generalized Masing Approach to Modeling Hysteretic Deteriorating Behavior," ASCE J. Engg. Mechanics, **133**(5), pp. 495- 505.

[14] Hou, J.F., Bai, H.B., and Li, D.W., 2008, "Damping Capacity Measurement of Elastic Porous Wire-Mesh Material in Wide Temperature Range," J. Matl. Proc. Tech., **206**, pp. 412-418.

[15] Ertas, B. H, and Luo, H., 2008, "Nonlinear Dynamic Characterization of Oil-Free Mesh Dampers," ASME J. Eng. Gas Turbines Power, **130**, pp. 032503-(1-8).

[16] Ertas, B. H., 2009, "Compliant Hybrid Journal Bearings using Integral Wire Mesh Dampers," ASME J. Eng. Gas Turbines Power, **131** (2), pp. 022503-(1-11).

[17] Pinkus, O., 1987, "The Reynolds Centennial: A Brief History of the Theory of Lubrication," ASME J. Trib., **109**, pp. 1-20.

[18] Blok, H. and van Rossum, J. J., 1953, "The Foil Bearing – A New Departure in Hydrodynamic Lubrication," Lub. Eng., **9**(6), pp. 316-320.

[19] DellaCorte, C., and Valco, M.J., 2000, "Load Capacity Estimation of Foil Air Journal Bearings for Oil-Free Turbomachinery Applications," NASA/TM-2000-209782.

[20] DellaCorte, C., 1997, "A New Foil Air Bearing Test Rig for use to 700° C and 70,000 rpm," NASA/TM-107405.

[21] DellaCorte, C., Lukaszewics, V., Valco, M.J., Radil, K.C., and Heshmat, H., 2000, "Performance and Durability of High Temperature Foil Air Bearings for Oil-Free Turbomachinery," Technical Report, NASA/TM-2000-209187/REV1.

[22] Radil, K., Howard, S., and Dykas, B., 2002, "The Role of Radial Clearance on the Performance of Foil Air Bearings," Technical Report, NASA/TM-2002-211705.

[23] DellaCorte, C., Radil, K. C., Bruckner, R. J., and Howard, S. A., 2008, " Design, Fabrication, and Performance of Open Source Generation I and II Compliant Hydrodynamic Gas Foil Bearings," Tribol. Transactions, **51**, pp. 254-264.

[24] Peng, Z.-C., and Khonsari, M. M., 2004, "On the Limiting Load-Carrying Capacity of Foil Bearings," ASME J. Tribol., **126**, pp. 817-818.

[25] Kim, T.H., and L. San Andrés, 2006, "Limits for High Speed Operation of Gas Foil Bearings," ASME J. Tribol., **128**, pp. 670-673.

[26] DellaCorte, C., Zaldana, A., and Radil, K., 2003, "A System Approach to the Solid Lubrication of Foil Air Bearing for Oil-Free Turbomachinery," ASME J. Tribol., **126**(1), pp. 200-207.

[27] Jahanmir, S., Heshmat, H., and Heshmat, C., 2009, "Evaluation of DLC Coatings for High-Temperature Foil Bearing Applications," ASME J. Tribology, **131**, pp. 011301-(1-11).

[28] Dodge, H.L., 1913, "The Change in the Elasticity of a Copper Wire with Current and External Heating," AIP Journal of Physical Review, **2**, pp. 431-449.

[29] Boyd, J. E., 1917, *Strength of Materials*, McGraw-Hill Book Company, New York.

[30] San Andrés, L., Kim, T.H., Ryu, K., Chirathadam, T. A.,Jarrett, C., Hagen, K., Martinez, A., Rice, B., Niedbalski, N., Hung, W., and Johnson, M., "Gas Bearing Technology for Oil-Free Microturbomachinery – Research Experience for Undergraduate (REU) Program at Texas A&M University," ASME Paper No. GT2009-59920.

[31].Childs, D., 1993, *Turbomachinery Rotordynamics: Phenomena, Modeling, & Analysis*, John Wiley & Sons, New York.

[32].Coleman, H.W., and Steele, G.W., 1998, *Experimentation and Uncertainty Analysis for Engineers*, John Wiley & Sons, New York.

[33]. Bently, D.E., Hatch, C.T, and Grissom, B, 2002, *Fundamentals of Rotating Machinery Diagnostics*, Bently Pressurized Bearing Press, Minden, NV, pp. 138.

APPENDIX A

CALIBRATION OF EDDY CURRENT SENSOR AND SPRING CONSTANT

Figures A.1 and A.2 display the calibration curves for a mechanical spring (torque measurement) and an eddy current sensor (aluminum target). A dynamometer applies a force on the steel spring and the eddy current sensor measures the corresponding deflection. The estimated spring constant is 879.5 N/m. The gain of the eddy current sensor for the aluminum target, 13.446 V/mm, is estimated using the displacement reading from a positioning table digital readout and the corresponding eddy current sensor voltage due to the aluminum target displacement.
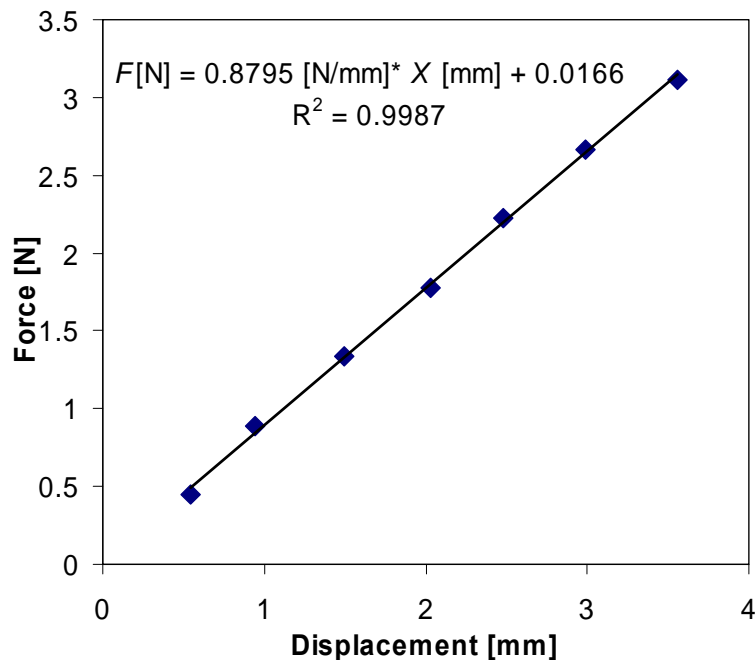

F[N] = 0.8795 [N/mm]* X [mm] + 0.0166
R^2 = 0.9987

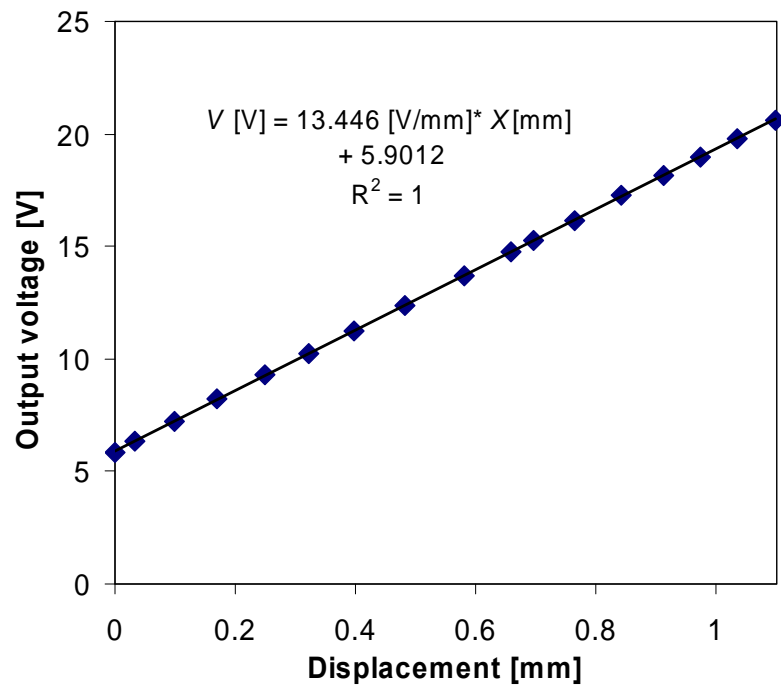**Fig. A.1 Force versus displacement (Calibration of spring for torque measurement)**

Fig. A.2 Calibration of eddy current sensor (3300 XL) for aluminum target

APPENDIX B

UNCERTAINTY ANALYSIS

EDDY CURRENT SENSOR CALIBRATION

The proximity sensor calibration uses displacement reading from a positioning table digital readout ($U_d = \pm 0.0005$ mm) and a voltmeter ($U_v = \pm 0.005$ V). The eddy current proximity sensor gain follows the relationship

$$G = \frac{\Delta D}{\Delta V_{fit}} \tag{B.1}$$

where ΔD is the change in displacement for a change in voltage, $\Delta V_{fit,}$, resulting from the linear fit. The general equation for computing the uncertainty of parameters [32] for a typical expression, $r = f(x_1, x_2, ...x_n s)$, is defined as

$$U_r = \sqrt{(\frac{\partial r}{\partial x_1} U_{x_1})^2 + (\frac{\partial r}{\partial x_1} U_{x_2})^2 + ... + (\frac{\partial r}{\partial x_n} U_{x_n})^2} \tag{B.2}$$

The uncertainty of expression B.1, using equation B.2 becomes

$$(\frac{U_G}{G})^2 = (\frac{\partial G}{\partial D} \frac{U_D}{D})^2 + (\frac{\partial G}{\partial V_{fit}} \frac{U_{fit}}{G})^2 = (\frac{1}{\Delta D} \frac{U_D}{D})^2 + (\frac{1}{\Delta V_{fit}} \frac{U_{V_{fit}}}{})^2 \tag{B.3}$$

where ΔD and ΔV_{fit} are the range of experimental values and $U_{V_{fit}}$ is computed from the uncertainty of the voltmeter and the uncertainty of the curve fit as described

$$U_{V_{fit}} = \sqrt{(U_{fit})^2 + (U_V)^2} \tag{B.4}$$

Hence, G = 13.44 ± 0.007 V/mm

CALIBRATION OF SPRING CONSTANT

The spring[5] constant calibration uses displacement reading from a positioning table digital readout ($U_d = \pm 0.0005$ mm) and a force gauge ($U_f = \pm 0.2$ N). The spring constant follows the relationship

---

[5] For measurement of drag torque

$$K = \frac{\Delta F}{\Delta D_{fit}} \tag{B.5}$$

The uncertainty of expression B.5, using equation B.2 becomes

$$(\frac{U_K}{K})^2 = (\frac{\partial K}{\partial F} \frac{U_F}{F})^2 + (\frac{\partial K}{\partial D_{fit}} \frac{U_{fit}}{K})^2 = (\frac{1}{\Delta F} \frac{U_F}{F})^2 + (\frac{1}{\Delta D_{fit}} \frac{U_{D_{fit}}}{})^2 \tag{B.6}$$

Where ΔF and ΔD_{fit} are the range of experimental values and $U_{D_{fit}}$ is computed from the uncertainty of the displacement measurement and the uncertainty of the curve fit as described

$$U_{D_{fit}} = \sqrt{(U_{fit})^2 + (U_D)^2} \tag{B.7}$$

Thus, K = 0.88 ± 0.03 N/mm

TORQUE MEASUREMENT

The torque measurement follows the relationship

$$T = V\, G\, K\, L \tag{B.8}$$

where, T is the bearing torque, V the voltmeter reading, G the Eddy current sensor gain, K the spring constant, and L the torque arm length. The uncertainty of expression B.8, using equation B.2 becomes

$$(\frac{U_T}{T})^2 = (\frac{U_V}{V})^2 + (\frac{U_G}{G})^2 + (\frac{U_K}{K})^2 + (\frac{U_L}{L})^2 \tag{B.9}$$

The uncertainty in the measurement of torque of 10 Nmm is ± 0.35 Nmm using eqn. (B.9)

IMPACT TEST

The uncertainty in the stiffness and damping coefficients are given by the instrumentation uncertainty associated with the measurements of relative bearing displacements, bearing cartridge acceleration, impact force and frequency in their respective expressions in eqn. (3) in Chapter V.

$$\left(\frac{U_K}{K}\right)^2 = \left(\frac{U_F}{F}\right)^2 + \left(\frac{U_{A_X}}{A_X}\right)^2 + \left(\frac{U_{A_Y}}{A_Y}\right)^2 + 3\left(\frac{U_X}{X}\right)^2 + 3\left(\frac{U_Y}{Y}\right)^2 + \left(\frac{U_M}{M}\right)^2 \qquad \text{(B.10)}$$

$$\left(\frac{U_C}{C}\right)^2 = \left(\frac{U_F}{F}\right)^2 + \left(\frac{U_{A_X}}{A_X}\right)^2 + \left(\frac{U_{A_Y}}{A_Y}\right)^2 + 3\left(\frac{U_X}{X}\right)^2 + 3\left(\frac{U_Y}{Y}\right)^2 + \left(\frac{U_M}{M}\right)^2 + \left(\frac{U_\omega}{\omega}\right)^2 \qquad \text{(B.11)}$$

where,

$$\left(\frac{U_F}{F}\right) < 0.02 \ (2\ \%\ \text{linearity}), \quad \left(\frac{U_{A_X}}{A_X} = \frac{U_{A_Y}}{A_Y}\right) < 0.01 \ (1\ \%\ \text{linearity}),$$

$\left(\dfrac{U_\omega}{\omega}\right) < 0.05$ for frequencies > 50 Hz, uncertainties associated with the displacement and mass measurements are negligibly small.

APPENDIX C

FULL SPECTRUM CASCADE PLOTS OF ORBITS OF BEARING DISPLACEMENTS RELATIVE TO THE ROTATING SHAFT

Figure C.1 shows a representation of a rotor bearing system, and the directions of high and low stiffnesses. Also, note that the attitude angle of the rotor is a function of the rotor speed and the total applied load. Hence, the direction with higher stiffness may not be along the direction of the net static load, but differs from it as much as the attitude angle. The MMFB responses relative to the rotating shaft in the horizontal and vertical directions are recorded using two eddy current sensors affixed to the bearing cartridge, as shown in Figure C.1.

Note that, the total static load on the bearing cartridge comprises of the applied pull loads in the horizontal direction (3.5 N, 8.9 N and 17.8 N) and the weight of the bearing assembly (3.5 N). The turbocharger shaft is manually accelerated to speeds above 60,000 rpm. During deceleration to rest, the bearing motions are recorded using ADRE® data acquisition system.
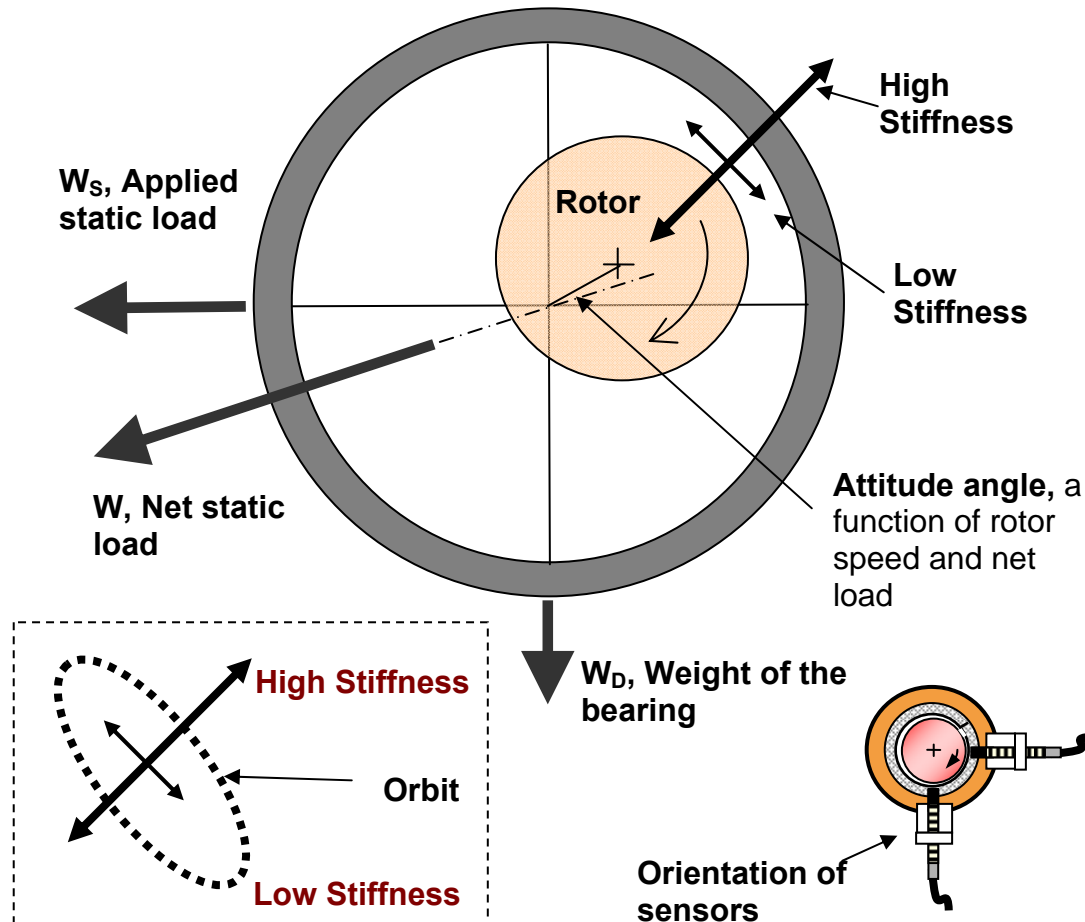
Fig. C.1 Representation of MMFB stiffnesses while the bearing is airborne

Figure C.2 shows the FFT of the transient response of the test journal (alone), affixed on the shaft stub of the turbocharger driven test rig, detailed in Chapter III, for an impact load on the turbocharger center housing along the vertical direction. An accelerometer is affixed on the test journal to measure the responses corresponding to the impulse force. The measured journal response shows the presence of two natural frequencies for the overhung journal, around 160 Hz (~ 10 krpm) and 580 Hz (~35 krpm).
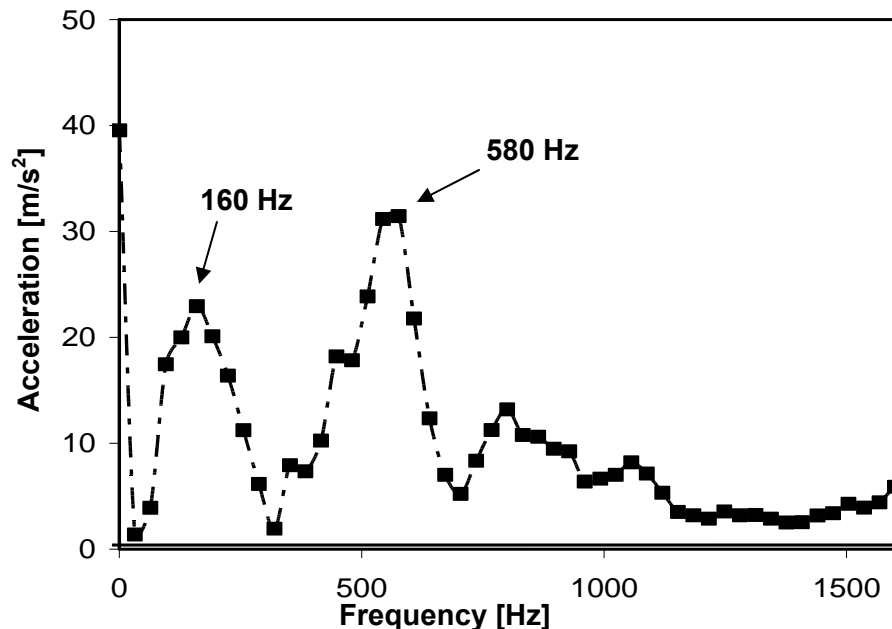
Fig. C.2 FFTs of transient responses of test journal to impact forces on the turbocharger center housing. Average of five impacts. Test Journal not rotating

Figure C.3 shows the full spectrum cascade plots of the orbit of shaft motion. A static load of 3.5 N is applied in the horizontal direction. The full spectrum cascade plot aids to identify whether the bearing cartridge vibration is forward or backward in relation to the shaft rotation [33]. The full spectrum plot is derived using the waveforms recorded by the eddy current sensors along two orthogonal directions, providing the knowledge of the direction of precession at every speed. With increasing unidirectional loading, the 1*X* and 2*X* forward whirl component magnitudes decrease, and the reverse whirl component magnitudes increase, causing a reverse precession. The magnitude of the reverse whirl component is related to the degree of ellipticity of the orbit. The cascade plot shows the presence of small amplitude 2*X* components and subsynchronous motion above 30 krpm (MMFB airborne). Note the large synchronous amplitude around 35 krpm, accompanied by subsynchronous (~ 100 Hz) excitations (encircled in Figure C.3), as the rotor traverses one of its natural frequencies. Similarly, when the rotor speed is ~ 10 krpm (160 Hz), the bearing displacement amplitudes are high.
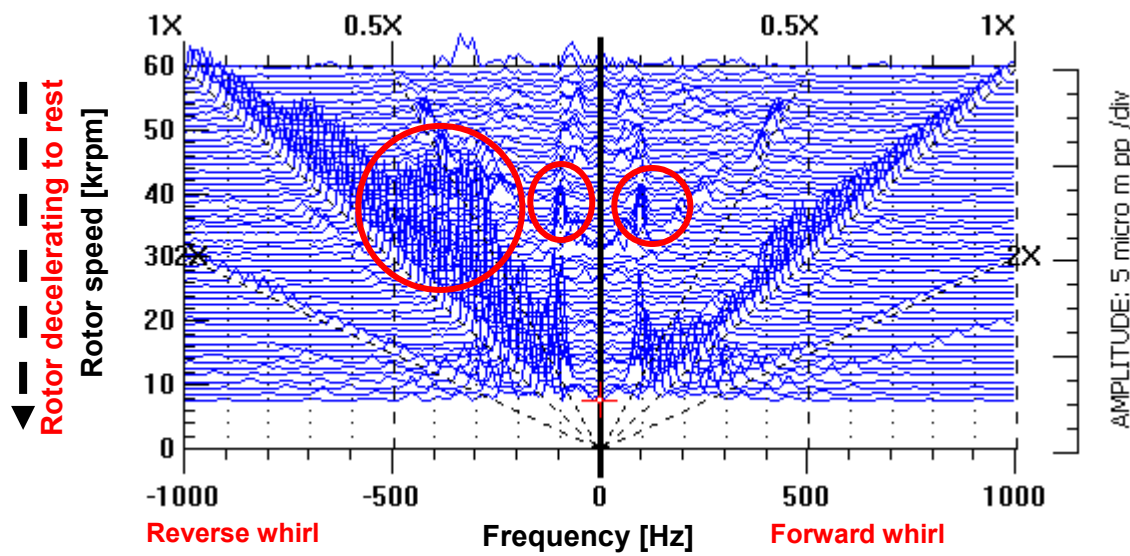
Fig. C.3 Full spectrum cascade plot of the orbit of shaft motion. Applied static load of 3.5 N in the horizontal direction. Bearing weight of 3.5 N

Figure C.4 shows the rotor unfiltered orbits at rotor speeds of 10, 20, 30, 40, 50 and 60 krpm, while a static horizontal load of 3.5 N is applied. The unfiltered orbits show the path of the shaft centerline relative to the pair of eddy current sensors affixed orthogonally on the bearing cartridge [33]. The shaft whirls in the reverse direction for rotor speeds above 50 krpm. At a shaft speed of 10 krpm, the total shaft motion combines both forward and reverse precessions. This is clearly identified from the 'loop' like shape of the orbit. Note that Figure C.8 later shows that the filtered 1X component of the shaft motion follows a backward whirl. The highly elliptical orbits are typical of radial loading.

10 krpm, 5 μm/div **20 krpm, 5 μm/div** **30 krpm, 5 μm/div**

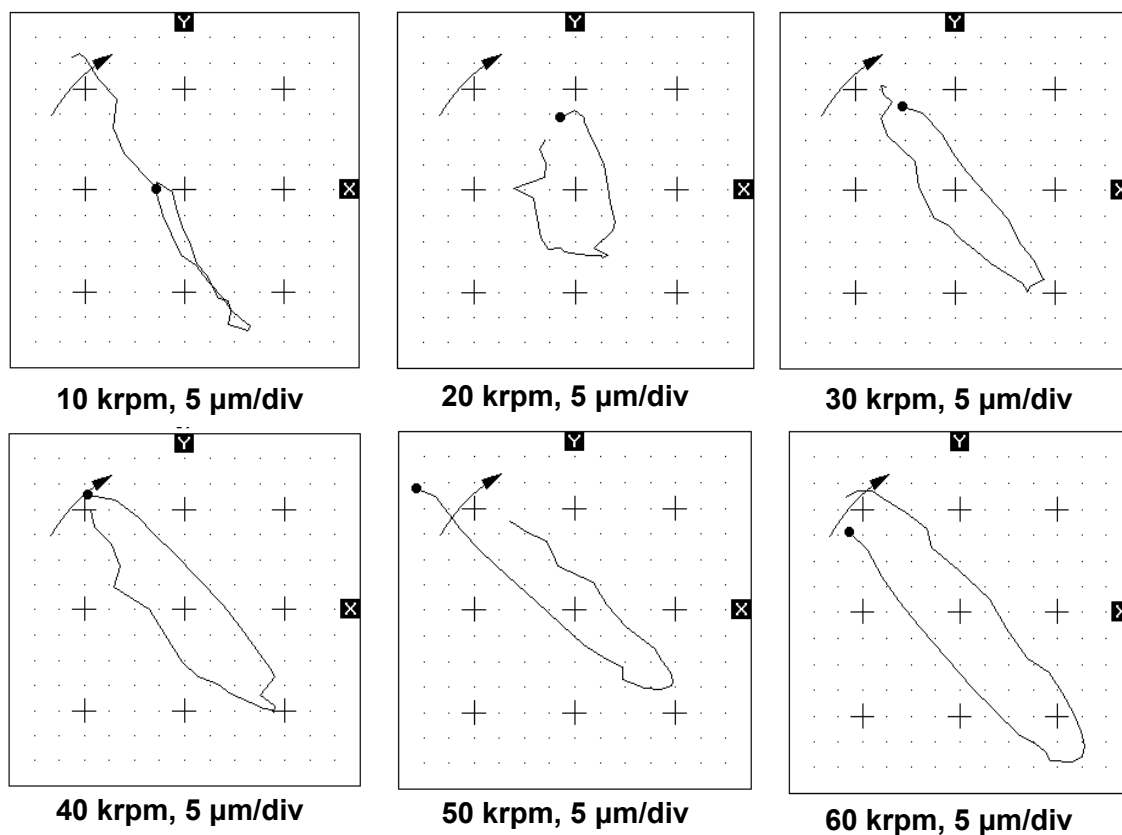**40 krpm, 5 μm/div** **50 krpm, 5 μm/div** **60 krpm, 5 μm/div**

Fig. C.4 Rotor unfiltered orbits at rotor speeds of 10, 20, 30, 40, 50 and 60 krpm. Applied static load of 3.5 N in the horizontal direction. Bearing weight of 3.5 N

Figure C.5 shows the cascade plot of the orbit of shaft motion with an applied horizontal load of 18 N. Although, there are small $2X$ components, any significant subsynchronous vibration at the highest rotor speed of 60 krpm is absent. The large amplitudes near 40 krpm are due to the excitation of a rotor natural frequency. Significant subsynchronous motion (~ 160 Hz) are recorded only while the rotor speed is 35 krpm (~ 580 Hz).

Figure C.6 shows the rotor unfiltered orbits at rotor speeds of 10, 20, 30, 40, 50 and 60 krpms with an applied horizontal load of 18 N. In contrast to a lightly loaded bearing, as in Figure C.4, the relative bearing displacements show backward whirl only at speeds above 60 krpm with a larger horizontal static load of 18 N. Significant subsynchronous

excitation (~ 160 Hz) continues to be present while the rotor traverses the journal natural frequency of ~ 580 Hz (35 krpm), even with a larger horizontal load
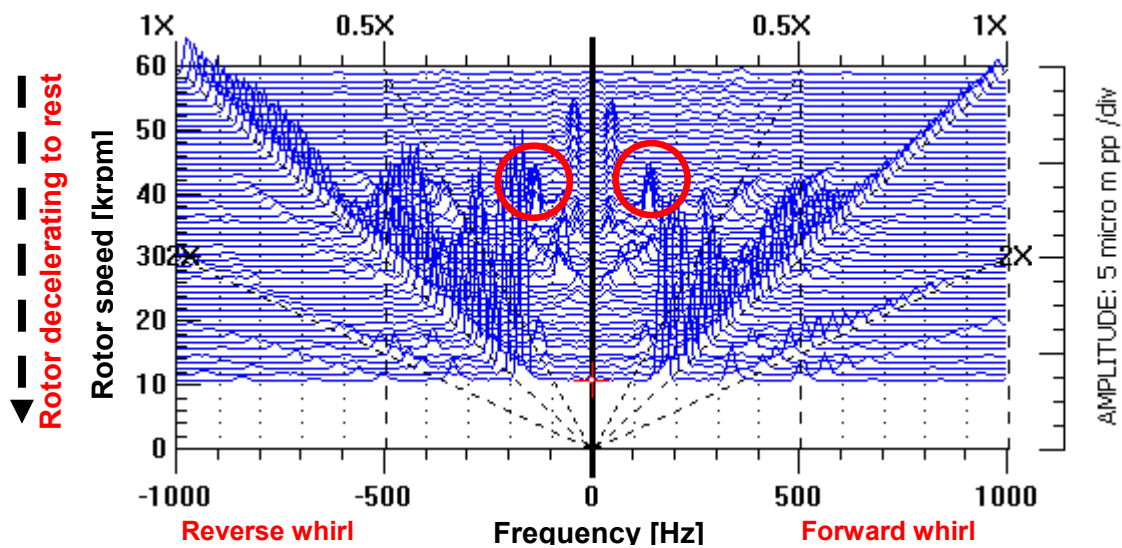

Fig. C.5 Full spectrum cascade plot of the orbit of shaft motion. Applied static load of 18 N (4lbf) in the horizontal direction. Bearing weight of 3.5 N
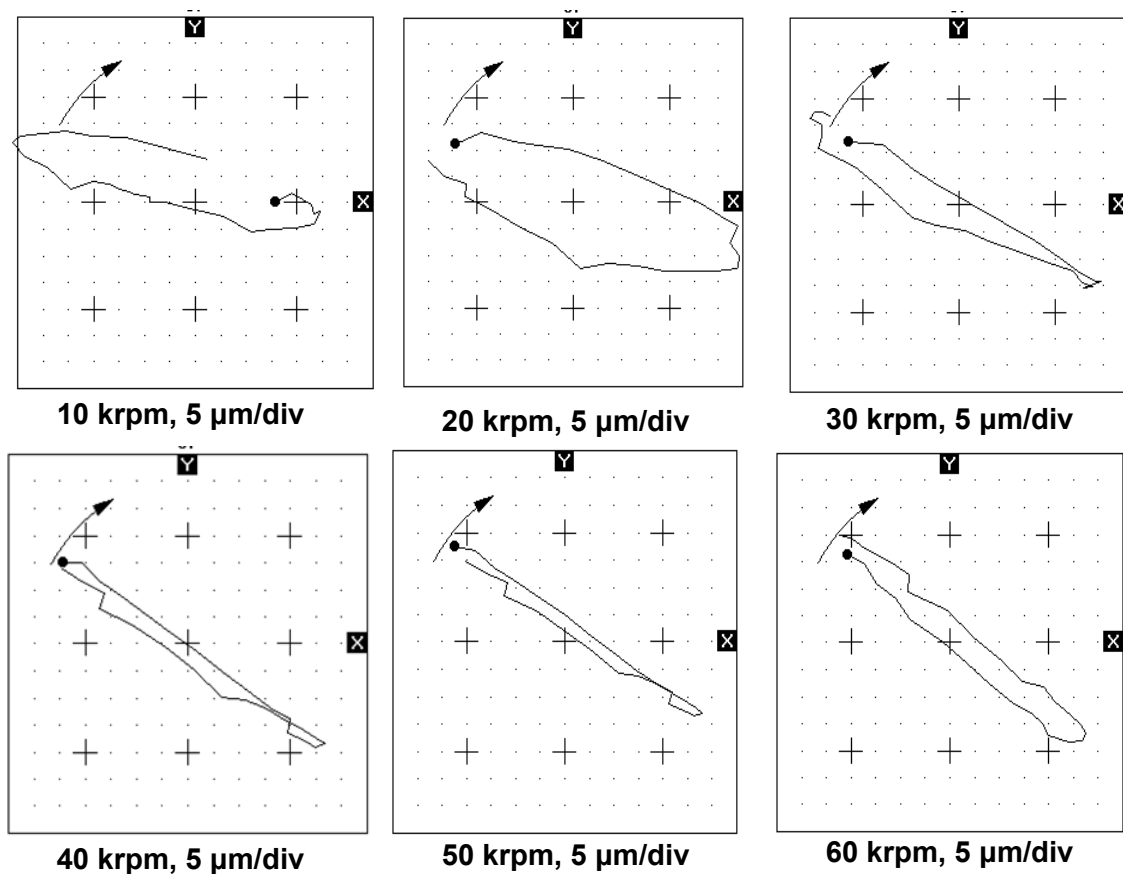
Fig. C.6 Rotor unfiltered orbits at rotor speeds of 10, 20, 30, 40, 50 and 60 krpm. Applied static load of 18 N in the horizontal direction. Bearing weight of 3.5N

Figures C.7 and C.8 shows the full spectrum cascade plots of the signals from the accelerometers affixed on the bearing cartridge. The bearing cartridge motion shows less subsynchronous components compared to the relative bearing displacements. However, amplitudes of vibration near the rotor natural frequencies 580 Hz (~ 35 krpm) and 160 Hz (~ 10 krpm) are prominent.

Figures C.9-11 show the synchronous speed rotor orbits with applied static loads of 3.5 N, 9 N and 18 N, respectively. The 1X filtered orbits show that, as the applied horizontal load increases, the onset speed of reverse whirl increases. With an applied horizontal load of 3.5 N, the rotor whirls backwards at speeds of 10 krpm, and also

above 50 krpm. However, as the horizontal load increases to 18 N, the backward whirl around 10 krpm is absent. Also, the rotor shows reverse precession only at speeds around 60 krpm with a larger static load of 18 N.
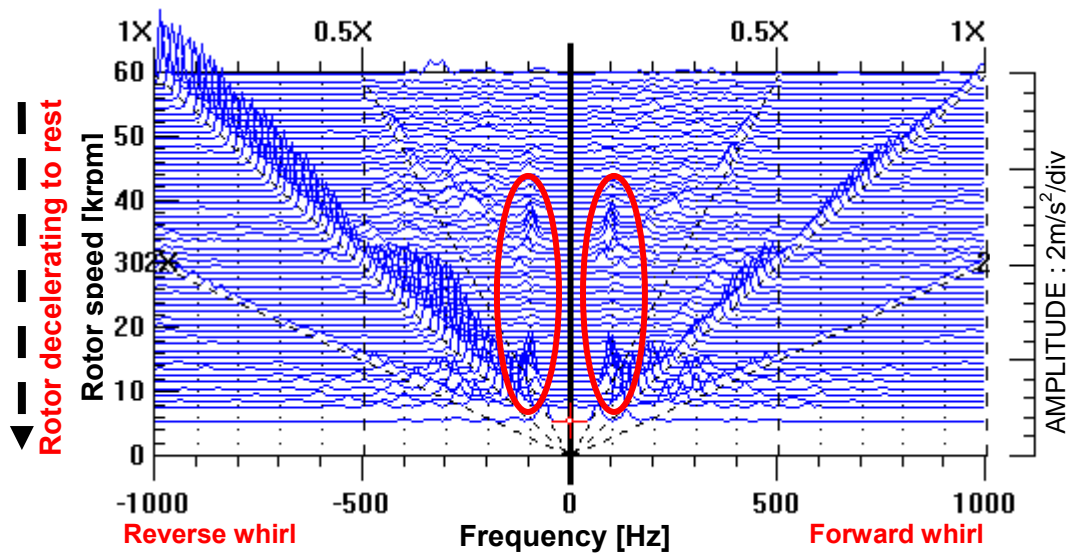

Fig. C.7 Full spectrum cascade plot of the accelerometer signals. Applied static load of 3.5 N in the horizontal direction. Bearing weight of 3.5 N
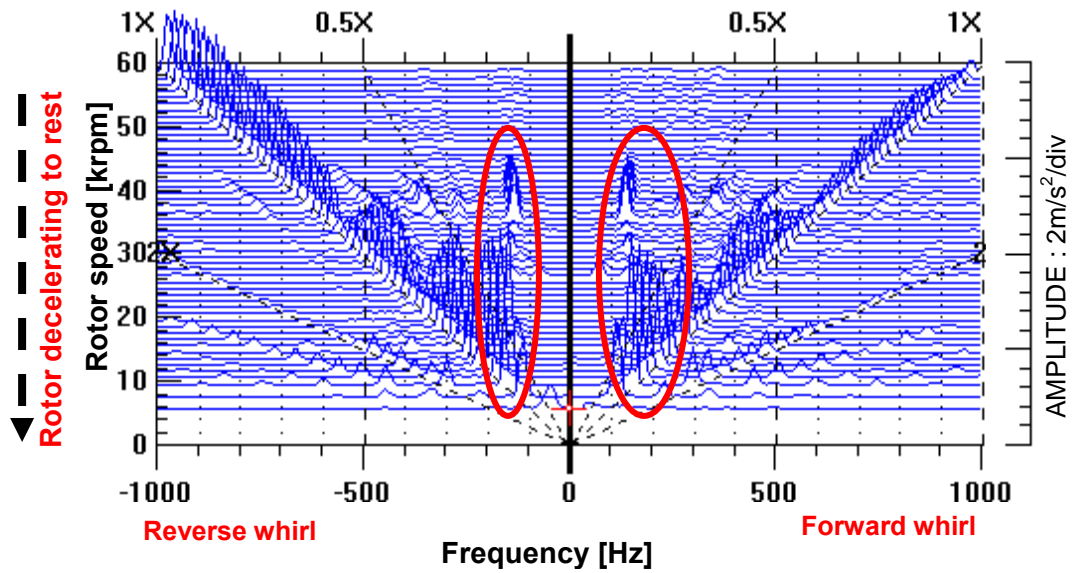
Fig. C.8 Full spectrum cascade plot of the accelerometer signals. Applied static load of 18 N (4lbf) in the horizontal direction. Bearing weight of 3.5 N
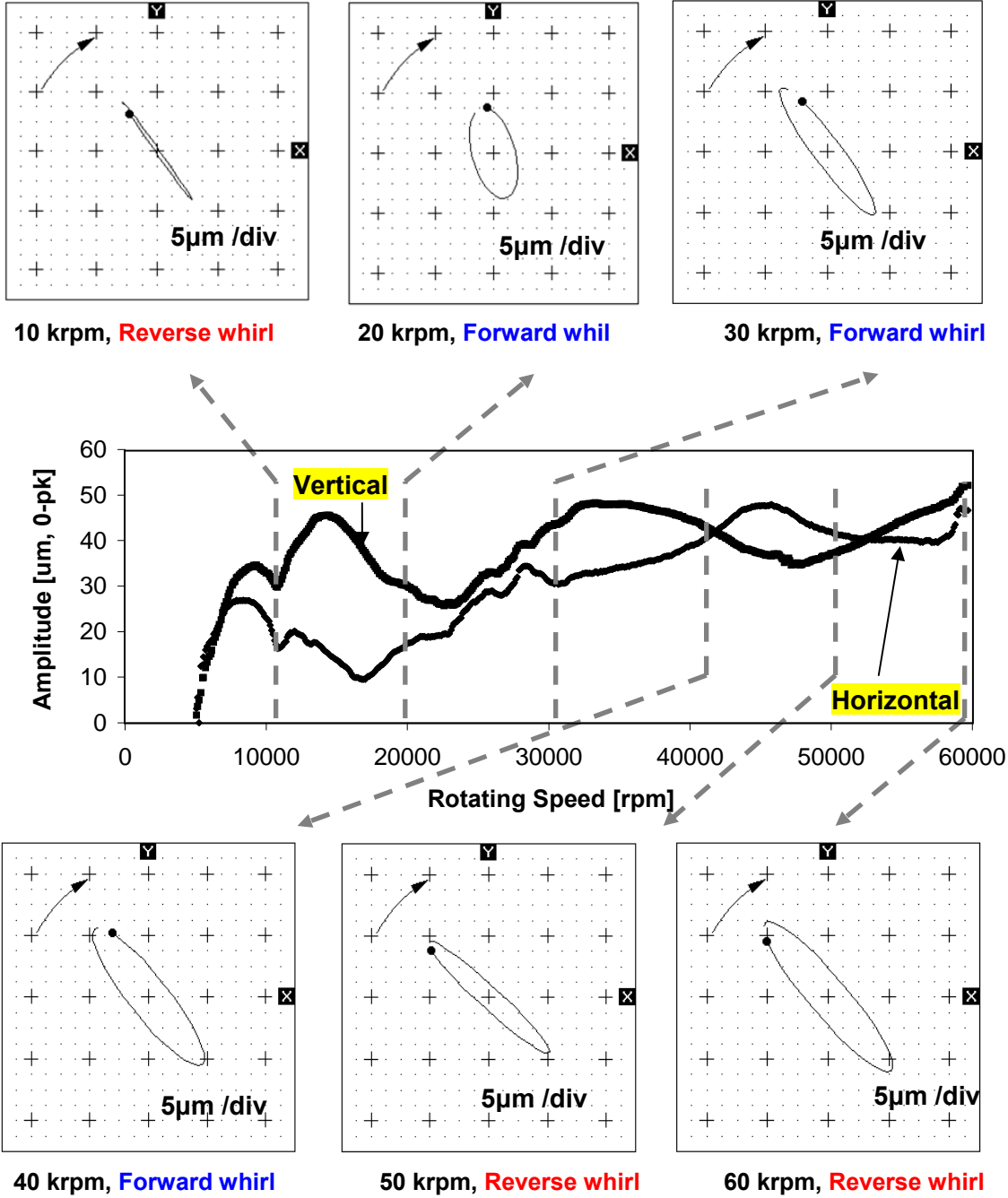
Fig. C.9 Synchronous speed rotor orbits at 10, 20, 30, 40, 50 and 60 krpm. Applied static loads of 3.5 N in the horizontal direction. Bearing weight of 3.5 N. Slow roll compensation at 5000 rpm
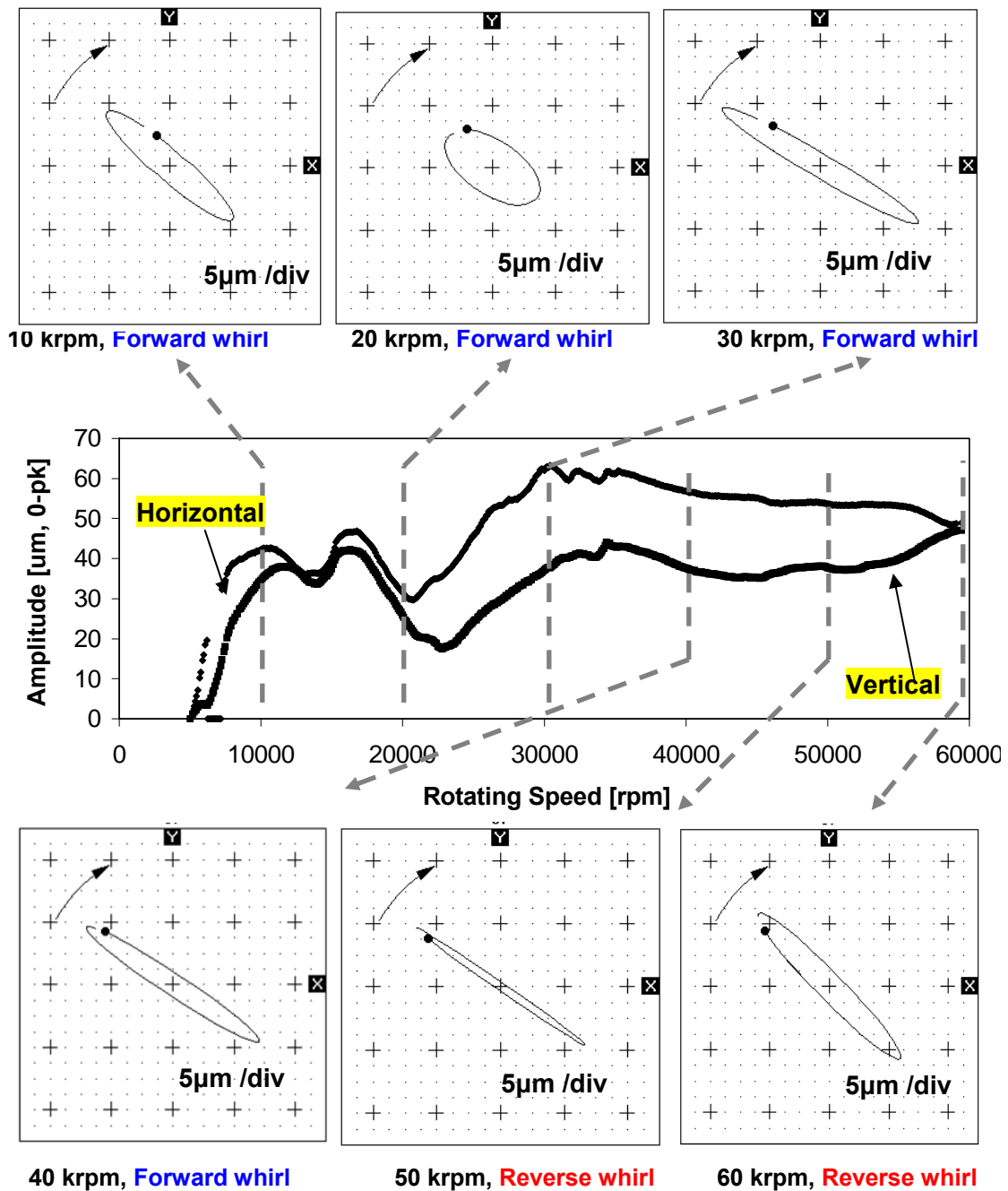
Fig. C.10 Synchronous speed rotor orbits at 10, 20, 30, 40, 50 and 60 krpm. Applied static loads of 9 N in the horizontal direction. Bearing weight of 3.5 N. Slow roll compensation at 5000 rpm
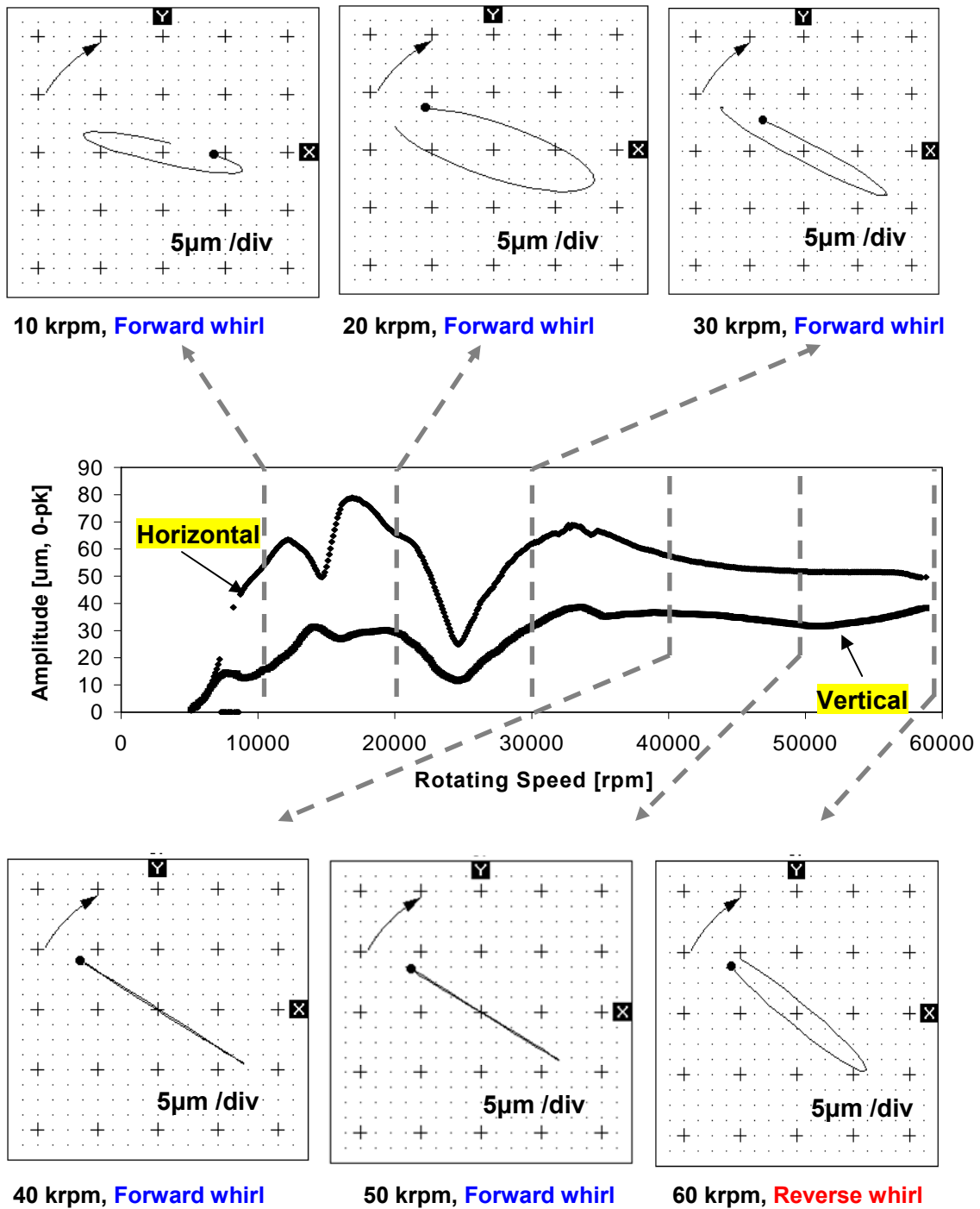
Fig. C.11 Synchronous speed rotor orbits at 10, 20, 30, 40, 50 and 60 krpm. Applied static loads of 18 N in the horizontal direction. Bearing weight of 3.5 N. Slow roll compensation at 5000 rpm

APPENDIX D

VARIABILITY OF THE ESTIMATED STIFFNESS AND
EQUIVALENT VISCOUS DAMPING COEFFICIENTS

Impact load tests are conducted with i) no shaft rotation and ii) with the shaft rotating at 50 krpm (834 Hz). Stiffness and damping coefficients are identified from the frequency domain averages of ten impact forces and the respective bearing motion responses. To estimate the variability of the identified parameters, four sets of impact load tests are conducted for each case. Figure D.1 shows the identified MMFB stiffness without shaft rotation. The identified parameters show a maximum variability of 0.08 MN/m at the highest test frequency of 200 Hz. Within the frequency range 70-150 Hz, the variability is only 0.02 MN/m. The average variability over the frequency range 0-200 Hz is 0.034 MN/m.
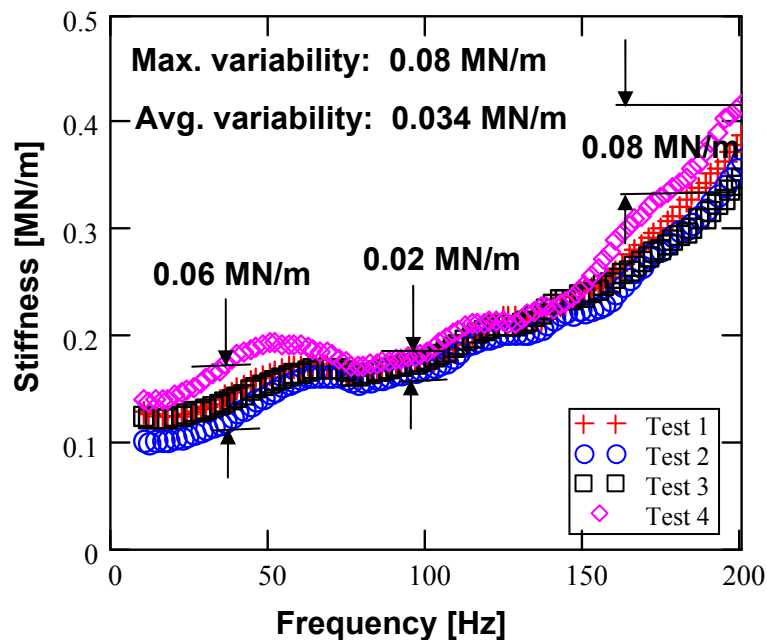

Fig. D.1 Variability of identified MMFB stiffnesses versus frequency. Shaft not rotating. Four test results

Figure D.2 shows the identified MMFB direct stiffness while the shaft rotates at 50 krpm (834 Hz). The identified parameters show a maximum variability of 0.05 MN/m around the frequency of 40 Hz. The average variability of the identified parameter in the frequency range 0 - 200 Hz is 0.026 MN/m. Figure D.3 shows the variability of the identified MMFB equivalent viscous damping coefficients without shaft rotation. The identified parameters show a maximum variability of 150 Ns/m around the frequency of 25 Hz. The average variability for the frequency range 0 – 200 Hz is 35 Ns/m.
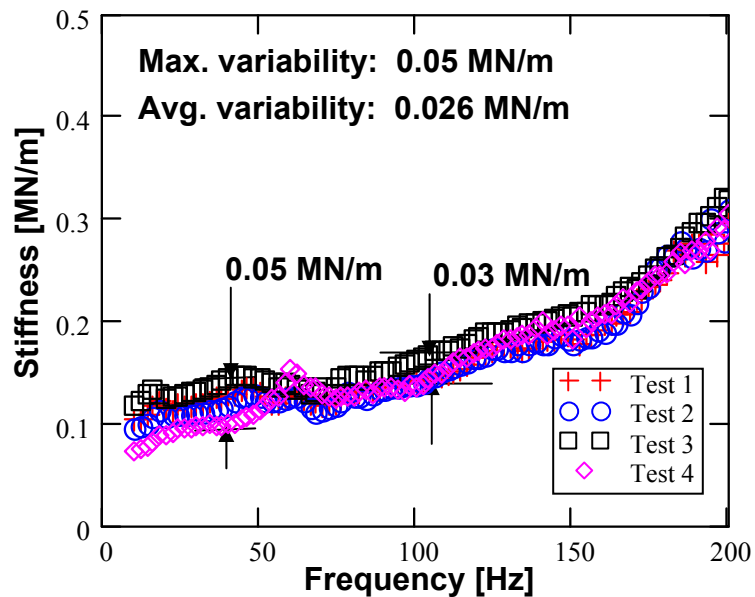

Fig. D.2 Variability of identified MMFB direct stiffnesses versus frequency. Shaft rotating at 50 krpm (834 Hz). Four test results
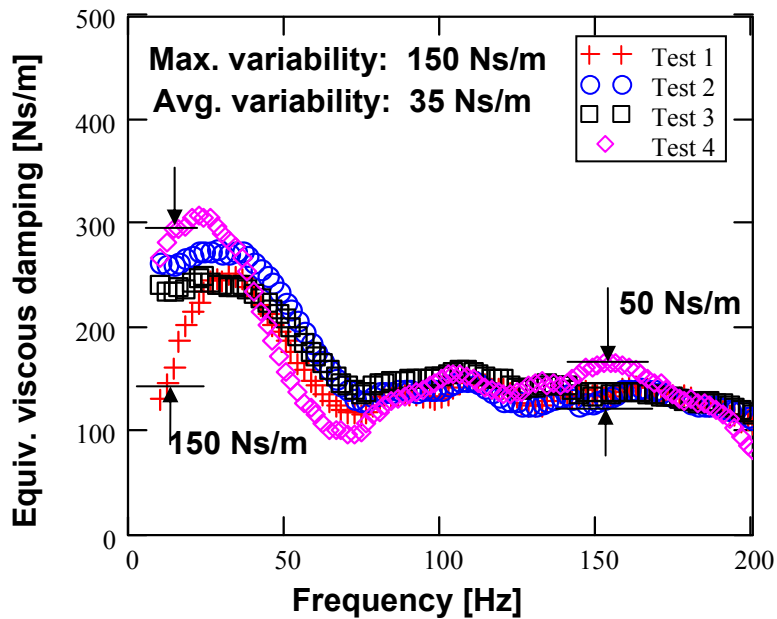
Fig. D.3 Variability of identified MMFB equivalent viscous damping versus frequency. Shaft not rotating. Four test results

Figure D.4 shows the variability of the identified MMFB equivalent viscous damping coefficients while the shaft rotates at 50 krpm. The identified parameters show a maximum variability of 180 Ns/m around the frequency of 25 Hz. The average variability is 54 Ns/m for the frequency range of 0-200 Hz.
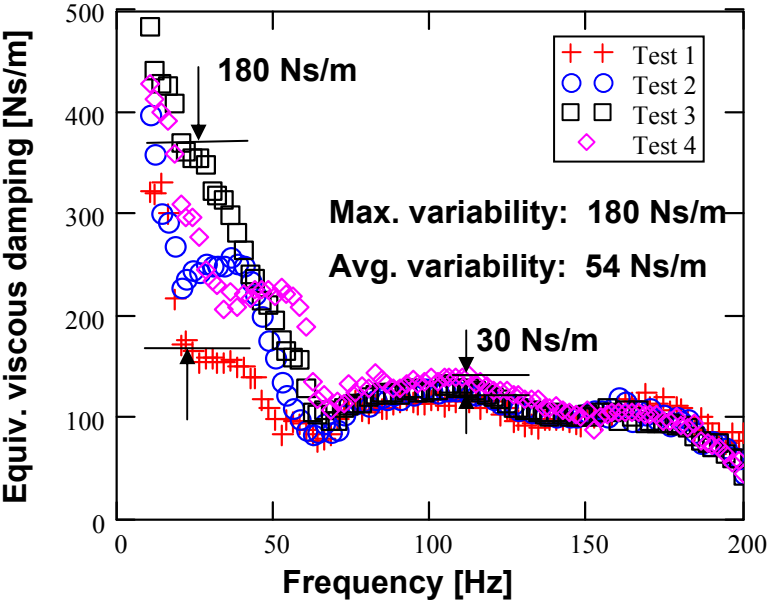
Fig. D.4 Variability of identified MMFB equivalent viscous damping versus frequency. Shaft rotating at 50 krpm (834 Hz). Four test results

VITA

Name:	Thomas Abraham Chirathadam
PermanentAddress:	Chirathadam House, Kundukulam Road, Mannuthy PO, Thrissur, Kerala, INDIA 680651
Email Address:	vintace@gmail.com
Web Address:	http://www.thomasabraham.com
Education:	B.Tech., Mechanical Engineering, National Institute of Technology Calicut, India, 2005
	M.S., Mechanical Engineering, Texas A&M University College Station, TX, 2009
Employment:	Larsen & Toubro ltd., Mumbai, India, 2005-07